# Optimization of Biophotonics and Optomechanics for Frequency Domain Tissue Fluorescence Measurements

**by**
**Luwei Zou**

**A thesis submitted in partial fulfillment**
**of the requirements of the degree of**
**Master of Science in Engineering**
**(Mechanical Engineering)**
**in the University of Michigan-Dearborn**
**2017**

**Master's Thesis Committee:**

**Assistant Professor Joe Fujiou Lo, Chair**
**Assistant Professor Mathumai Kanapathipillai**
**Associate Professor Yasha Yi**

# Acknowledgements

I would like to thank Prof. Joe Fujiou Lo for his support and mentoring of my thesis. I would also like to thank Rui Liu for finishing the early ground works that went into this thesis. Moreover, I thank the members of Dr. Lo's Lab for their assistance and friendship throughout my studies in University of Michigan at Dearborn: Rui Liu, Mengyang Zhou, Zhengtuo Zhao, Di Hu, Kai Duan, Mohammed-Baker Habhab, Tania Ismail and Jessica Hallgath. I would also like to thank University of Michigan-Dearborn for the financial support.

# Table of Contents

# List of Figures

# List of Tables

# List of Abbreviations

| | |
|---|---|
| FD | Frequency domain |
| ECM | Extra cellular matrix |
| PMT | Photomultiplier tube |
| DSO | Digital storage oscilloscope |
| APD | Avalanche photodiode |
| FAD | Flavin adenine dinucleotide |
| FITC | Fluorescein isothiocyanate |
| 9CA | 9-Anthracenecarboxylic acid |
| DC | Direct current |
| DLP | Digital light processing |
| CAD | Computer-aided design |
| FEA | Finite element analysis |
| PLA | Polylactic acid |
| ABS | Acrylonitrile butadiene styrene |
| NA | Numerical aperture |
| UV | Ultraviolet |
| FFT | Fast Fourier transform |
| NADH | Nicotinamide adenine dinucleotide |
| AGEs | Advanced glycation end-products |
| FWHM | Full width at half max |
| CCD | Charge-coupled device |
| PBS | Phosphate-buffered saline |
| FLIM | Fluorescence-lifetime imaging microscopy |

# Abstract

Collagens and extra cellular matrix (ECM) proteins play important roles in the structural composition of tissues, and their modifications are implicated in diseases including cancer metastasis, tissue fibrosis, diabetic ulcers. Current tissue collagen analyses are based on destructive histological methods, whereas the ECM proteins' intrinsic autofluorescences can provide a label-free detection and imaging to differentiate tissue compositions, modifications, and disease states. Fluorescence lifetime spectroscopy has been demonstrated as a key technique to distinguish ECM proteins in tissue. However, the large, expensive, and often operationally challenging instrumentation required to measure fluorescent lifetimes from tissues prevents the technique from gaining traction in biomedical applications.

To this end, this thesis represents three major efforts to address this roadblock in tissue lifetime instrumentation by 1) demonstrate a facile fluorescence lifetime technique via frequency domain analysis, 2) realizing a hand-held multispectral lifetime probe for point detection on the skin, 3) realizing a low-cost, low complexity LED based imaging system to enable FLIM (fluorescence lifetime imaging microscopy) for histology without daunting instrumentation.

In the first effort, the frequency domain (FD) fluorescence lifetime technique was demonstrated for the differentiation of collagens I/III and elastin, three major biophotonic components in wound tissues that undergo change during healing. In the second effort, a compact multispectral

system demonstrated the FD lifetime's utility as a point-of-care device, and added additional wavelength-specific lifetime spectroscopy to further improve differentiation. The third effort expands the FD technique to an imaging modality, by leveraging LED scanning optomechanics to create histological images of tissues without labeling. Additionally, the scanning of a diabetic ulcer showed evidence that the technique can provide quantitative information on disease modification of the tissue that current immunohistochemical methods are ill-equipped to provide. By providing a quantitative, more nuance model of tissue biophotonics while using low-cost, low complexity FD instrumentation, the works in this thesis hopes to increase accessibility and popularity of label-free ECM lifetime spectroscopy for a number of biomedical and clinical applications.

**Keywords:**

Optomechanics, autofluorescence, frequency domain, 3D printing, collagen, elastin, wound healing, diabetes, advanced glycation end products, LED, FLIM

# Chapter 1 Overall Introduction

Collagen composition in the tissue's extra cellular matrix (ECM) varies during many processes such as cancer metastasis, wound healing, fibrosis, and aging. In wound healing, specifically, ECM is disrupted by the act of wounding and injury. In addition, the proliferation and remodeling phase of wound healing involves a change from immature type III collagen to the stronger type I collagen [1-4]. Monitoring collagen transition during these processes, then, can provide important information about wound maturity and strength. Current techniques to visualize and quantify changes in tissue collagen types rely on immunohistochemistry and polarized picrosirius staining under the microscope [5-8]. Novel methods such as laser-induced fluorescence and multiphoton excitation are becoming popular as label-free detection techniques, which have already been applied to ocular, skin, and liver tissue microscopies [9-17], in addition to our work on differentiating collagen types via fluorescence lifetimes [18].

**Collagen and ECM Composition of Skin Wounds Tissue**

In skin wounds, collagen remodeling occurring underneath a closing wound cannot be easily assessed by visual monitoring. The primary structural component of normal dermis is mostly collagen, with elastin, glycoproteins, and glycosaminoglycans also present. During the proliferation phase, fibroblasts proliferate in the wound and produce ECM, especially collagens, to replace the provisional matrix formed in homeostasis/inflammatory stage of the earlier wound healing process to establish scar tissue [4]. Normal skin and wounds that have undergone collagen remodeling contain more mature cross-linked collagen I fibers, while

immature wounds contain more parallel collagen III fibers [5, 6]. Elastin is another major molecule of ECM produced by fibroblasts and smooth muscle cells, which provide resilience to the skin and other tissues. It is abnormally expressed during skin wound healing which partially contributes to the impaired breaking strength of scars compared with unwounded skin [7]. Restoration of normal ECM architecture is necessary for skin wounds to gain the tensile strength that is required to maintain tissue integrity [1]. Full thickness murine wounds have been used as important models to study wound healing, including collagen remodeling processes.

**Characteristics of Collagen and Tissue Autofluorescence**

Autofluorescence from collagen (i.e. without staining) is commonly observed in cell and tissue microscopy. The major collagen fluorophores are lysine derived pyridinium, tyrosine, and phenylalanine groups [8-11], which can be affected by crosslinking, glycation, and their compositions in different types of collagens [12-14]. Collagen autofluorescence, in combination with other endogenous fluorophores, can provide differentiation between normal and cancerous tissues [15, 16], promising tumor demarcation in minimally invasive surgeries [17, 18]. Moreover, collagen fiber orientation and crystallinity enable second harmonic generation (SHG) using laser induced autofluorescence [19-23]. Both multiphoton collagen autofluorescence and SHG have been adapted for monitoring skin aging [24, 25] and investigating ocular pathology [26-30]. Despite the ability to detect endogenous fluorophores—e.g. NADH+, elastin, and collagen—no differentiation of collagen types using SHG and multiphoton microscopy has been demonstrated. This is because very little differences exist in the spectral domain of collagen types, e.g. I versus III. However, autofluorescences from different collagen types evidently have strong differences in the time domain [31, 32]—their lifetimes are significantly different and sensitive to the crosslinking and

glycation, as mentioned earlier. Therefore, fluorescence lifetime spectroscopy, either in the time-domain or frequency domain, can provide non-invasive differentiation of collagen types in tissue.

**Time and frequency domain lifetime for collagen**

Collagen and elastin autofluorescence, and fluorescence in general, can be modeled as a linear, time-invariant system with a characteristic impulse response function specific to a particular fluorophore [33-35]. Therefore, the input (excitation) and output (emission) of such a system can be considered in time and frequency domains. In the time domain, the input excitation is convolved with the impulse response to yield the emission intensity over time. This time domain method has been demonstrated with sub-nanosecond pulsed lasers and fast photomultiplier tube (PMT) detectors to reconstruct collagen fluorescence impulse response decays, with associated lifetime constants [36-39]. While the time domain method obtains more information over shorter pulses, the cost of the pulsed lasers, triggering electronics, and PMT detectors, in addition to the complexity of the system, prevent its wider use in biomedical applications. On the other hand, frequency domain method preserves the modulation frequency of the sinusoid, while changing the modulation amplitude and phase as a function of the specific fluorophore's impulse response decay. This is analogous to a linear time-invariant system encountered in electrical circuits. Frequency domain technique is a lower complexity, cost-effective alternative for monitoring biological tissues compared to time domain method [17, 18]. Optimum modulation frequencies for tissue structural proteins like collagens and elastin range from 10-100 MHz [19]. This lowers requirements for the LED driver electronics, photodetector amplifier responses, and signal digitization and recording speeds [20, 21]. A single, portable USB multi-channel digital storage oscilloscope (DSO) can perform the acquisitions for both the excitation and emissions waveforms. Using the phase $\Delta\phi$ and

modulation m from oscilloscope measurements, two lifetimes can be calculated and combined via multi-exponential models, at particular wavelengths, to find characteristic lifetimes of a sample.

$$\tau_\phi = \omega^{-1} \tan \Delta\phi \qquad (1)$$

and

$$\tau_m = \omega^{-1}(m^{-2} - 1)^{1/2} \qquad (2)$$

In this study, the characteristic lifetimes of collagens at three wavelength bands were quantified to provide the ability for spectral-lifetime discrimination.

**References**


1. J.R. Merkel, B.R. DiPaolo, G.G. Hallock, D.C. Rice. Type I and type III collagen content of healing wounds in fetal and adult rats. Proceedings of the Society of Experimental Biology and Medicine 1988;187:493-497.

2. P.G. Watson, R. Young. Scleral structure, organization, and disease. A review. Experimental Eye Research 2004;78:609-623.

3. R. Beuerman, A. Aplkama, J. Reynaud, N. Nguyen, H. Kikuchi, R. Kalia. Three-dimensional structure of the laminar cribrosa of the living eye. Proceedings of SPIE 2001;4431. doi:10.1117/12.447402.

4. I.A. Darby, T.D. Hewitson. Fibroblast differentiation in wound healing and fibrosis. International Review of Cytology 2007;257:143-179.

5. H.P. Ehrlich. The role of connective tissue matrix in wound healing. Prog. Clin. Biol. Res. 1988;266:243–258.

6. M.J. Ranzer, L. Chen, L.A. DiPietro. Fibroblast function and wound breaking strength are impaired by acute ethanol intoxication. Alcohol Clin. Exp. Res. 2011;35:83-90.

7. J.F. Almine, S.G. Wise, A.S. Weiss. Elastin signaling in wound repair. Birth Defects Res. C. Embryo Today 2012;96(3):248-257.

8. Z. Deyl, K. Macek, M. Adam, O. Vancíková. Studies on the chemical nature of elastin fluorescence. Biochim. Biophys. Acta. 1980;625(2):248-254.

9. D.R. Eyre, M.A. Paz, P.M. Gallop. Cross-linking in collagen and elastin. Annual Review of Biochemistry 1984;53:717-748.

10. E. Fujimori. Changes induced by ozone and ultraviolet light in type I collagen: Bovine Achilles tendon collagen versus rat tail tendon collagen. Eur. J. Biochem. 1985;152:299-306.

11. O. Vančíková, Z. Deyl. Disappearance of tyrosine residues in collagen with age. Suggestion of a possible reaction mechanism. Experimental Gerontology 1974;9(3):123–130.

12. I. Miksík, Z. Deyl. Change in the amount of epsilon-hexosyllysine, UV absorbance, and fluorescence of collagen with age in different animal species. J. Gerontol. 1991;46(3):B111-1116.

13. V.M. Monnier, R.R. Kohn, A. Cerami. Accelerated age-related browning of human collagen in diabetes mellitus. PNAS 1984;81(2):583-587.

14. R. Meerwaldt, T. Links, R. Graaff, S.R. Thorpe, J.W. Baynes, J. Hartog, R. Gans, A. Smit. Simple noninvasive measurement of skin autofluorescence. Ann. N. Y. Acad. Sci. 2005;1043:290–298.

15. N. Kollias. In vivo fluorescence spectroscopy of nonmelanoma skin cancer. Photochemistry and Photobiology 2001;73(2):178–183.

16. P. Yang, W. Wang, G. Tang. R.R. Alfano. Changes of collagen and nicotinamide adenine dinucleotide in human cancerous and normal prostate tissues studied using native fluorescence spectroscopy with selective excitation wavelength. J. Biomed. Opt. 2010;15(4):047008. doi:10.1117/1.3463479.

17. S. Andersson-Engels, J. Johansson, K. Svanberg, S. Svanberg. Fluorescence imaging and point measurements of tissue: applications to the demarcation of malignant tumors and atherosclerotic lesions from normal tissue. Photochemistry and Photobiology 1991;53(6):807–814.

18. P.J. Tadrous, J. Siegel, P.M.W. French, S. Shousha, E. Lalani, G.W.H. Stamp. Fluorescence lifetime imaging of unstained tissues: early results in human breast cancer. The Journal of Pathology 2003;199(3):309–317.

19. V. Lutz, M. Sattler, S. Gallinat, H. Wenck, R. Poertner, F. Fischer. Characterization of fibrillar collagen types using multi-dimensional multiphoton laser scanning microscopy. International Journal of Cosmetic Science 2012;34:209–215.

20. E. Kable, A. Jones, I. Fraser, F. Manconi, M.D. Gorrell. 3-Dimensional imaging of collagen using second harmonic generation Guy Coxa. Journal of Structural Biology 2003;141(1):53–62.

21. A. Zoumi, A. Yeh, B.J. Tromberg. Imaging cells and extracellular matrix in vivo by using second-harmonic generation and two-photon excited fluorescence. PNAS 2002;99(17):11014–11019. doi: 10.1073/pnas.172368799.

22. E. Brown, T. McKee, E. diTomaso, A. Pluen, B. Seed, Y. Boucher, R.K. Jain. Dynamic imaging of collagen and its modulation in tumors in vivo using second-harmonic generation. Nature Medicine 2003;9(6):796-800.

23. K. König, K. Schenke-Layland, I. Riemann, U.A. Stock. Multiphoton autofluorescence imaging of intratissue elastic fibers. Biomaterials 2005;26(5):495–500.

24. L. Brancaleon, A.J. Durkin, J.H. Tu, G. Menaker, J.D. Fallon, S. Lin, S. Jee, J. Chan, R. Wu, W. Lo, H. Tan, W. Lin, J. Chen, T. Young, C. Hsu, C. Dong. Monitoring photoaging by use of multiphoton fluorescence and second harmonic generation microscopy. Proc. SPIE 2006;6078. doi:10.1117/12.647009.

25. J. Adur, L. DSouza-Li, M.V. Pedroni, C.E. Steiner, V.B. Pelegati, A.A. de Thomaz, H.F. Carvalho, C.L. Cesar. The severity of Osteogenesis imperfecta and type I collagen pattern in human skin as determined by nonlinear microscopy: proof of principle of a diagnostic method. PLoS One 2013;8(7):e69186. doi: 10.1371/journal.pone.0069186.

26. S. Teng, H. Tan, J. Peng, H. Lin, K.H. Kim, W. Lo, Y. Sun, W. Lin, S. Lin, S. Jee, P.T.C. So, C. Dong. Multiphoton autofluorescence and second-harmonic generation imaging of the ex vivo porcine eye. Invest. Ophthalmol. Vis. Sci. 2006;47(3):1216-1224.

27. P. Matteini, F. Ratto, F. Rossi, R. Cicchi, C. Stringari, D. Kapsokalyvas, F.S. Pavone, R. Pini. Photothermally-induced disordered patterns of corneal collagen revealed by SHG imaging. Optics Express 2009;17(6):4868-4878.

28. P. Steven, M. Müller, N. Koop, C. Rose, G. Hüttmann. Comparison of cornea module and dermaInspect for noninvasive imaging of ocular surface pathologies. J. Biomed. Opt. 2009;14(6):064040. doi: 10.1117/1.3275475.

29. P. Steven, M. Hovakimyan, R.F. Guthoff, G. Hüttmann, O. Stachs. Imaging corneal crosslinking by autofluorescence 2-photon microscopy, second harmonic generation, and fluorescence lifetime measurements. J. Cataract Refract. Surg. 2010;36(12):2150-2159. doi: 10.1016/j.jcrs.2010.06.068.

30. G. Deka, W. Wu, F. Kao. In vivo wound healing diagnosis with second harmonic and fluorescence lifetime imaging. J. Biomed. Opt. 2013;18(6):061222.

31. P. Ashjian, A. Elbarbary, P. Zuk, D.A. Deugarte, P. Benhaim, L. Marcu, M.H. Hedrick. Noninvasive in situ evaluation of osteogenic differentiation by time-resolved laser-induced fluorescence spectroscopy. Tissue Engineering 2004;10(3-4):411-420.

32. L. Marcu, D. Cohen, J.M.I. Maarek, W.S. Grundfest. Characterization of type I, II, III, IV, and V collagens by time-resolved laser-induced fluorescence spectroscopy. Proc. SPIE 2000;3917. doi:10.1117/12.382720.

33. J.R. Lakowicz. Principle of Fluorescence Spectroscopy, third ed. Springer Science & Business Media, 2006.

34. D. Elson, J. Requejo-Isidro, I. Munro, F. Reavell, J. Siegel, K. Suhling, P. Tadrous, R. Benninger, P. Lanigan, J. McGinty, C. Talbot, B. Treanor, S. Webb, A. Sandison, A. Wallace, D. Davis, J. Lever, M. Neil, D. Phillips, G. Stamp, P. French. Time-domain fluorescence lifetime imaging applied to biological tissue. Photochem. Photobiol. Sci. 2004;3:795-801.

35. K. Dowling, M.J. Dayel, M.J. Lever, P.M. W. French, J.D. Hares, A.K.L. Dymoke-Bradshaw. Fluorescence lifetime imaging with picosecond resolution for biomedical applications. Optics Letters 1998;23(10):810-812.

36. M.Y. Berezin, S. Achilefu. Fluorescence lifetime measurements and biological imaging. Chem. Rev. 2010;110(5):2641–2684.

37. J.E. Phipps, Y. Sun, M.C. Fishbein, L. Marcu. A fluorescence lifetime imaging classification method to investigate the collagen to lipid ratio in fibrous caps of atherosclerotic plaque. Lasers Surg. Med. 2012;44(7):564-571. doi: 10.1002/lsm.22059.

38. Y. Yuan, J. Hwang, M. Krishnamoorthy, K. Ye, Y. Zhang, J. Ning, R. C. Wang, M. J. Deen, Q. Fang. High-throughput acousto-optic-tunable-filter-based time-resolved fluorescence spectrometer for optical biopsy. Optics Letters 2009;34(7):1132-1134.

# Chapter 2 Compact, Non-invasive Frequency Domain Lifetime Differentiation of Collagens and Elastin in Wound and Ocular Tissue

## Introduction

### Collagen and ECM Composition of Ocular Tissue

In the eye, the type and orientation of collagen fibers vary by region and are closely related to the eye's functions [2, 4, 5]. For example, in the peripapillary region where the optic nerve exits the sclera, there is a predominant circumferential fiber alignment [6] that likely functions to control deformation and stress in the optic nerve head tissues. Similar to skin and other connective tissues, sclera is primarily composed of a matrix containing collagens, elastin [7], and proteoglycans [8]. The result is a tissue having strength and viscoelastic properties that help to protect the eye from severe loads, and also from brief elevations in intraocular pressure due to eye movements and other events such as rubbing. In the cornea, the lamellae are composed of collagen fibrils of uniform diameter running parallel to one another; however, in the sclera the collagen fibrils have varying diameter with an irregular branching pattern [9, 10]. Human eye tissue contains about 90% type I collagen and less than 5% type III collagen [2]. Levels of type III collagen in the bovine cornea average less than 1% in animals older than 3 months [11, 12]. Disorders in the ocular structure play a role in diseases such as glaucoma[13, 14] which manifests as damage to the tissues of the optic nerve head, and the corneal thinning disease keratoconus [15]. Structural problems of the sclera have also been implicated in myopia [16]. Abnormal elastin has been found in the lamina cribrosa tissue, which bridges the opening in the sclera at the optic nerve head, of glaucomatous eyes [16]. A noninvasive assay of tissue

would aid research into eye disorders such as these as well, as skin wounds discussed above, and could eventually be used as a diagnostic tool.

**System setup**

In this study, a general method is developed to detect and differentiate ECM proteins. Here, detections were demonstrated with type I collagen, type III collagen and elastin in the context of their measurements in skin wounds and ocular tissues [1-3]. The method uses a low cost, low complexity light emitting diode (LED) system to realize both non-invasive detection and specific discrimination of collagen and elastin variations in tissue. Modulated LED excitation was applied to frequency domain (FD) fluorescence lifetime spectroscopy to determine tissue autofluorescence lifetimes, Figure 1. It is shown that fluorescence lifetimes from collagen type I, collagen type III and elastin can be clearly distinguished. The extension of the method to detect other collagen types and ECM components is also discussed. Due to the low cost of LED and photodiode components, low complexity of the fiber optic probe, and the possibility of integrating phase and demodulation analyses on an integrated circuit, the developed technique is well suited to portable applications. Applications in implantable sensors, field diagnostics, and clinical monitoring can benefit from this technique to measure collagen and elastin distributions in biological tissues over time.

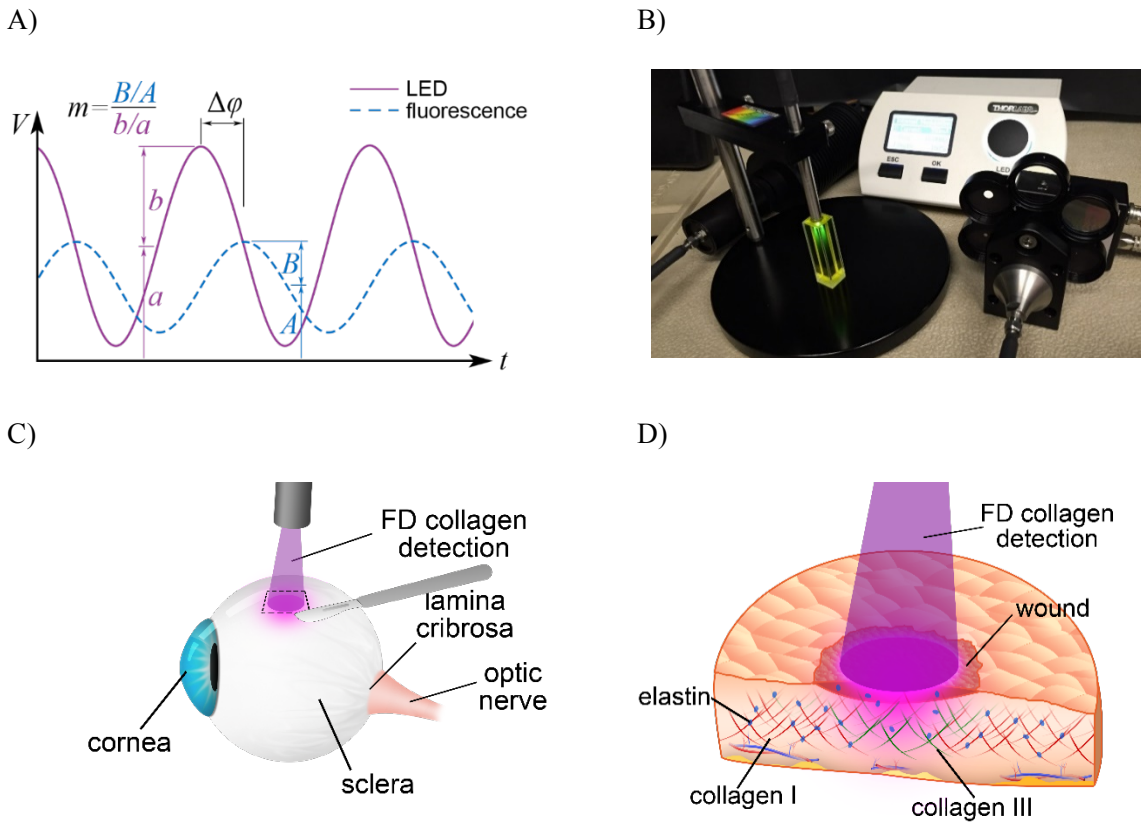


**Figure 1. Fiber based frequency domain collagen and elastin detection system.** A) Frequency domain fluorescence lifetime is based on the phase shift delay and amplitude demodulation of the fluorescence emission when a sample is excited by a modulated light source. B) The components of the systems are compact and cost-effective. This system can be applied to C) non-invasive probing of ocular tissue, and D) non-contact monitoring of wound healing. (Note that ocular and skin tissues were cut into samples and measured in this study.)

## Method

### FD ECM Detection System Overview

The system is composed of the following components: A modulated 365 nm wavelength LED (DC3100-365, Thorlabs, NJ) was used as the light source along with a 375 nm low-pass filter. This sinusoid modulated excitation light was carried by a 7 around 1 UV-resistant fiber probe (Stellarnet, FL) to illuminate the sample at frequencies from 10 MHz to 60 MHz. The emission and the reflected/scattered light from the sample were collected by the 7 fibers and the reflected/scattered light was then filtered by two 400 nm high pass filters. An avalanche photodiode (APD-110C, Thorlabs, NJ) picked up the filtered emission intensity and compared its modulation with the LED source on an oscilloscope, Figure 2. Because of the availability

of modulated LED, fast avalanche photodiode, and sub 100 MHz oscilloscope at affordable costs, the FD collagen system in this study does not require extra signal generator or heterodyne electronics [23, 24], and has a generally low overall system cost.

**System Optomechanics**

To couple the light from the LED, a plano-convex lens was used to collimate the light through the 375 nm low pass filter and focused by a second plano-convex lens onto the fiber probe. The fiber probe configuration has one illumination core in the center and 7 surrounding collection cores. This gives higher collection efficiency with smaller detection spot provided by the single illumination core. Similar to the LED coupling, detector coupling was achieved by collimating the collection fiber output through high pass filters. Then the signal was focused on the APD with a pair of plano-convex lenses (as shown in Figure 2). Moreover, the high pass filters, as well as neutral density filters, were mounted on a filter wheel to enable them to be moved in and out of the light path during normal and calibration operations. The components details and costs are listed in Table 1.

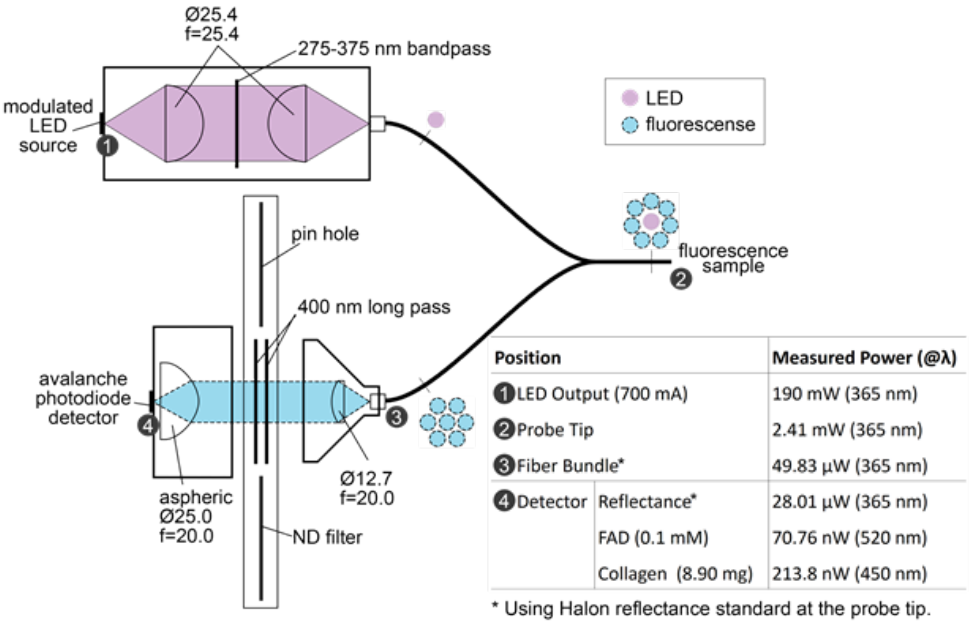


| Position | | Measured Power (@λ) |
|---|---|---|
| 1 LED Output (700 mA) | | 190 mW (365 nm) |
| 2 Probe Tip | | 2.41 mW (365 nm) |
| 3 Fiber Bundle* | | 49.83 µW (365 nm) |
| 4 Detector | Reflectance* | 28.01 µW (365 nm) |
| | FAD (0.1 mM) | 70.76 nW (520 nm) |
| | Collagen (8.90 mg) | 213.8 nW (450 nm) |

* Using Halon reflectance standard at the probe tip.

**Figure 2. FD ECM detection optomechanics design.** At the modulated LED light source, a pair of plano-convex lenses (ϕ25.4, f=25.4) help to couple light through an excitation filter (275-375 nm bandpass) into a 600 μm fiber. This excitation is illuminated on a fluorescence sample, and the emission is collected by seven 600 μm fibers into the detector coupling block. In the block, a plano-convex lens (ϕ12.7, f=20.0) collimates the emission intensity through a pair of 400 nm high pass filters, which can also be replaced by either a pin hole or a neutral density filter during calibration procedures. The filtered emission is then focused by an aspheric lens (ϕ25.0, f=20.0) onto a fast, avalanche photodiode. The efficiencies of the system can be interpreted by the optical power measured at various positions, as well as typical sample fluorescence from FAD and Collagen I.

**Table 1. System Components**

| Component | Relevant Spec | Price |
|---|---|---|
| Thorlabs Modulated LED Source | 700 mA, 10-90 MHz sinusoid | $2510 |
| 1” Lens tube components | SM1 lens tube, SM1 collimator | $450 |
| SM1 optics | 1” lens and lens tubes | $200 |
| Colored Glass Bandpass | 275-375 nm | $86 |
| Stellarnet 7 around 1 probe | 600 μm, solarization resistant | $600 |
| Manual filter wheel | 6 positions, 1” optics | $145 |
| Thorlabs Long pass FEL0400 | 400 nm | $73 (2) |
| Thorlabs APD120A2 Photodiode | DC-50 MHz (3dB), 2.5e6 V/W | $1070 |
| Rigol DS1000B Oscilloscope | 200 MHz, 2 GSa/s | $945 |

**System Calibration**

Phase shift and modulation depth ratio of the system were calibrated for comparisons between solid and liquid sample measurements. During these calibration measurements, the emission filters were switched out and replaced with neutral density filters or pin holes to further reduce intensity. For the reference phase angles, reflected/scattered light was measured at 10 to 60 MHz from frosted glass, water, and ethanol media to compare with measurements from powder/fiber form, aqueous solutions and ethanol solutions, respectively. For the reference modulation depth ratios, the LED waveform’s b/a ratios were measured for the frosted glass, water, and ethanol solutions, to parallel those measured for phase references.

**Fluorescence Standard, Purified Protein, and Tissue Sample Preparation**

For comparison to known lifetime standards, three fluorescence standards were measured:

flavin adenine dinucleotide (FAD), fluorescein isothiocyanate (FITC), and 9-Anthracenecarboxylic acid (9CA). 0.1 mM FAD was prepared in water while 0.1 mM FITC and 9CA were prepared in ethanol. FAD, fluorescein, and 9CA have lifetimes of 2.57, 3.94, and 11.75 ns, covering the range of lifetimes expected form the purified ECM proteins. Then, three purified ECM proteins were measured—collagen I, collagen III, and elastin—to represent important ECM components in ocular and skin tissues. Purified proteins were measured in solid powder or fiber forms. Finally, lifetime measurements were conducted in bovine sclera and cornea tissues, and murine normal and wound skin tissues (14 days post-wounding).

In this study, bovine tissue is used because it is plentiful and of similar consistency to human eye tissue and is often used as a precursor to experiments using cadaveric or surgical specimens of human origin [12, 25]. Bovine eyes were obtained from a local slaughterhouse and tested within 48 hours of the animal's death. Scleral and corneal tissues were dissected from the surrounding fat and extraocular muscles, then separated from the internal contents of the eye. The scleral and corneal tissues were then cut into 5 mm squares for measurement. Measurements were done normal to the external surface of the tissue samples.

BALB/C mice were used in the skin wound model. Murine experimental procedures followed the University of Illinois guidelines for the humane treatment of animals and were approved by the University of Illinois Institutional Animal Care and Use Committee. Wound models were created using 5 mm punch biopsies on day 0 and collected on day 14 post-wounding with 8 mm punch biopsies. Immediately after biopsy sampling, skin and wound tissues were measured normal to the external surface of the tissues.

**Frequency Domain Analysis**

During data acquisition, the raw emission signals were averaged 128 times in the oscilloscope to reduce effects of noise, then the averaged signals were imported into MATLAB (MathWorks,

MA) and fitted to sine functions. The least-square method was employed to fit the raw signals to a sine function with known frequencies.

$$y = a + b\sin(\omega x - \phi) \text{ , or } \quad y = A + B\sin(\omega x - \phi) \qquad (1)$$

Where ω is known when the sample is excited under the LED light with a certain frequency, x is the time axle, and y is the raw voltage data. The parameters phase ϕ, amplitude b, offset a for the excitation and phase ϕ, amplitude B, offset A for the emission waveforms (Figure 1A) are readily extracted from the curve fitting. However, there were noticeable DC offsets in the raw signals depending on measurement frequencies and oscilloscope settings. Therefore, DC offsets from dark readings (LED turned off) at specific measurement conditions were subtracted from the raw data before fitting and data processing. This process allowed more accurate calculations of the phase shift angles and modulation depths, without peak uncertainties, amplitude drifts, and waveform asymmetries from one part of the raw data to another, leading to better lifetime measurements.

After getting the phase angles and modulation depth ratios between 10 MHz to 60 MHz, the data was fitted to a multi-exponential model as described in [26], where the fluorescence impulse response function is assumed to be:

$$I(t) = \sum_{i=1}^{n} \alpha_i \mathrm{e}^{-t/\tau_i} \qquad (2)$$

Where $\alpha_i$ is the lifetime fraction of each component $\tau_i$ and $\sum \alpha_i = 1$. Thus $I(t)$ appears as a decay curve containing multiple exponents represented in the sample. The calculated phase shift angle$\phi_{c\omega}$ and modulation $m_{c\omega}$ can then be obtained from the sine $N_\omega$ and cosine $D_\omega$ transformation of $I(t)$:

$$N_\omega = \frac{\int_0^\infty I(t)\sin\omega t dt}{\int_0^\infty I(t)dt} \qquad (3)$$

$$D_\omega = \frac{\int_0^\infty I(t)\cos\omega t dt}{\int_0^\infty I(t)dt} \qquad (4)$$

Where their numerical values can be calculated by:

$$N_\omega \cdot J = \sum_{i=1}^{n} \frac{\alpha_i \omega \tau_i^2}{1+\omega^2 \tau_i^2} \qquad (5)$$

$$D_\omega \cdot J = \sum_{i=1}^{n} \frac{\alpha_i \tau_i}{1+\omega^2 \tau_i^2} \qquad (6)$$

Where $J = \sum \alpha_i \tau_i$.

Thus, the phase shift angle $\phi_{c\omega}$ and modulation $m_{c\omega}$ can be described by:

$$\phi_{c\omega} = \arctan(N_\omega / D_\omega) \qquad (7)$$

$$m_{c\omega} = (N_\omega^2 + D_\omega^2)^{1/2} \qquad (8)$$

An error-weighted $\chi^2$ sum of the squares of the deviations between the measured and calculated values is minimized to find the best fitting of multi-exponential model.

$$\chi^2 = \sum_\omega \frac{1}{\sigma_\phi^2} (\phi_\omega - \phi_{c\omega})^2 + \sum_\omega \frac{1}{\sigma_m^2} (m_\omega - m_{c\omega})^2 \quad (9)$$

Where $\sigma_\phi$ and $\sigma_m$ are the typical uncertainties in the phase and modulation data, respectively. Respective standard deviations from their measurements were used to represent these uncertainties. A single exponential model was used for fluorescence standard FAD, fluorescein, and 9CA, to be consistent with other reported studies [58, 64, 69]. A two-exponential model was used for protein and tissue samples, where fractional $\alpha_1$, $\alpha_2$, and their respective $\tau_1$ and $\tau_2$were calculated by minimizing the $\chi^2$ function describing deviations of their $\phi_\omega$ and $m_\omega$ values.

**Data Processing**

The LED trigger and APD detector signals were acquired using a 200 MHz oscilloscope (Rigol DS1000B). The data was then loaded into Matlab (Mathworks) for analysis. The curve fitting module was used to fit a sinusoid using the data, at pre-defined frequencies corresponding to the LED excitation, e.g. 10, 20 MHz, etc. Curve fitting was chosen over Fourier Transform due to its simple implementation in Matlab, where the amplitude, DC offset, and phase shift can be directly extracted, without ambiguity. No obvious processing time penalties were observed

using this method. Future implementation of Fourier Transform, however, can be beneficial in an embedded data processing unit. After extraction of the phase and modulation parameters, they were implemented into a minimization function to fit into the appropriate single/multi-exponential model.

## Result and Discussion

To characterize the FD ECM detection system, the calibration results and fluorescence spectra of each standard, protein, and tissue samples were presented. Then, the FD phase shift and demodulation results were presented. Next, the single and multi-exponential fitted lifetimes were summarized in Tabulated form. Finally, the relationship between temporal resolution and sample detectivity was characterized to describe the sensitivity of the FD system.

### System Calibration Results

The phase angles of mirror/water/ethanol references were fairly close to each other, Figure 3A. As with phase references, modulation references did not change significantly among all samples, Figure 3B.

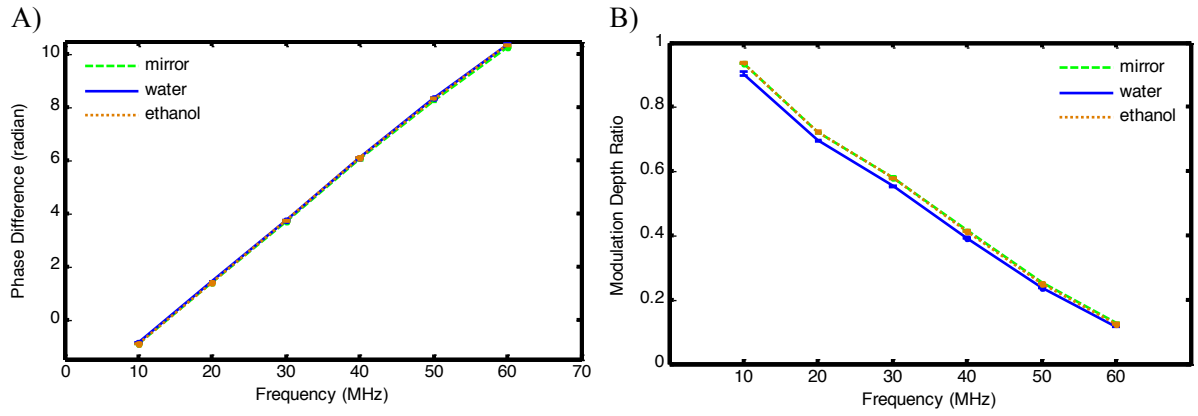


**Figure 3. References phase and modulation ratios.** A) Phase delays versus frequency of LED modulation. B) Modulation depth ratios versus frequency of LED modulation. Measurements were made using mirror/water/ethanol references to represent the solid, aqueous, and ethanol solvated samples. Error bar denotes standard deviation, n=3

**Spectral Domain Alone Cannot Distinguish Collagen Types and Elastin**

Spectral data showed that 9CA peaked at 450 nm, fluorescein at 520 nm, and FAD at 530 nm, Figure 4. Protein spectra generally overlapped for collagen I/III and elastin, but showed significant intensity differences above 450 nm. This spectral overlap, combined with other present chromophores like hemoglobin, makes tissue reflectance complicated and difficult to interpret. In the FD collagen system described in this manuscript, lifetime measurements were employed to distinguish purified protein components by integrating all wavelengths above 400 nm.

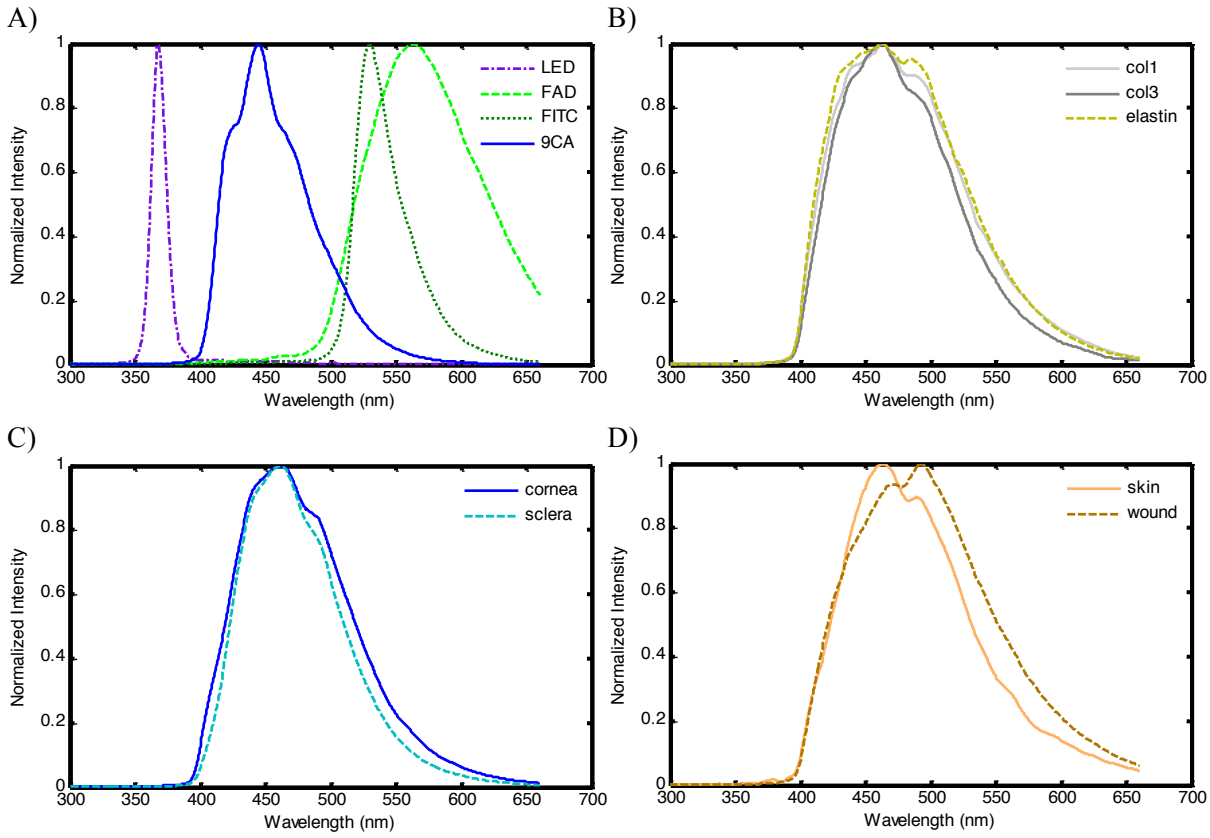


**Figure 4. Fluorescence spectra of standards, proteins, and complex tissue autofluorescence.** A) Emission spectra of standards with LED excitation spectra overlaid. B) Emission spectra of purified proteins samples. Emission spectra of C) ocular tissues samples and D) skin wound samples. Tissue samples have significant difference in the intensity above 450 nm that is complicated by multiple protein compositions. Standards were in 0.1mM concentration in their respective solvents; proteins in powder/fiber forms; and tissues cut into samples as described in the sample preparation section.

**Frequency Domain Phase Shift Results**

Phase shifts of the tested samples shown in Figure 5 were consistent with lifetimes of fluorescence standards and distinguished ECM proteins that comprise tissues. As seen in the figure, the phase shift angle rose with frequency as expected, following an inverse tangent profile consistent with equation (7). In general, larger phase shift translates to longer lifetime at a specific frequency. For the fluorescence standards, the phase shifts increased from FAD, fluorescein, to 9CA, in that order, Figure 5A. For the proteins, collagen I consistently measured smaller phase shifts than collagen III at all frequencies, while elastin measured larger phase shifts than the collagen samples, Figure 5B. For the bovine ocular tissues, the scleral tissue measured much larger phase shifts compared to corneal tissue, Figure 5C. The cornea is critical to the optical functions of the eye's lens and its transparency is the result of uniform diameter and arrangement of its collagen fibers [28, 29], whose crosslinking could be the cause of the smaller phase shift measurements. For the murine wound tissue, larger phase shifts were measured compared to normal skin tissue, indicative of longer lifetime components, Figure 5D. Compared to the collagen measurements, this difference may be due to the relatively greater amount of collagen III (larger phase shift) in the healing wound compared to normal skin [1]. It should be noted that multiple ECM proteins are present in the tissue samples, and collagen itself has multiple lifetime components. The multi-exponential decay model, described later, provided better fitting to extract lifetime information from these tissues. Additionally, the phase shift results showed that frequency band of 40-50 MHz has optimal separation for the protein and tissue samples, especially for skin wounds, where data from 10, 20, and 50 MHz overlaps and do not contribute to their separation.

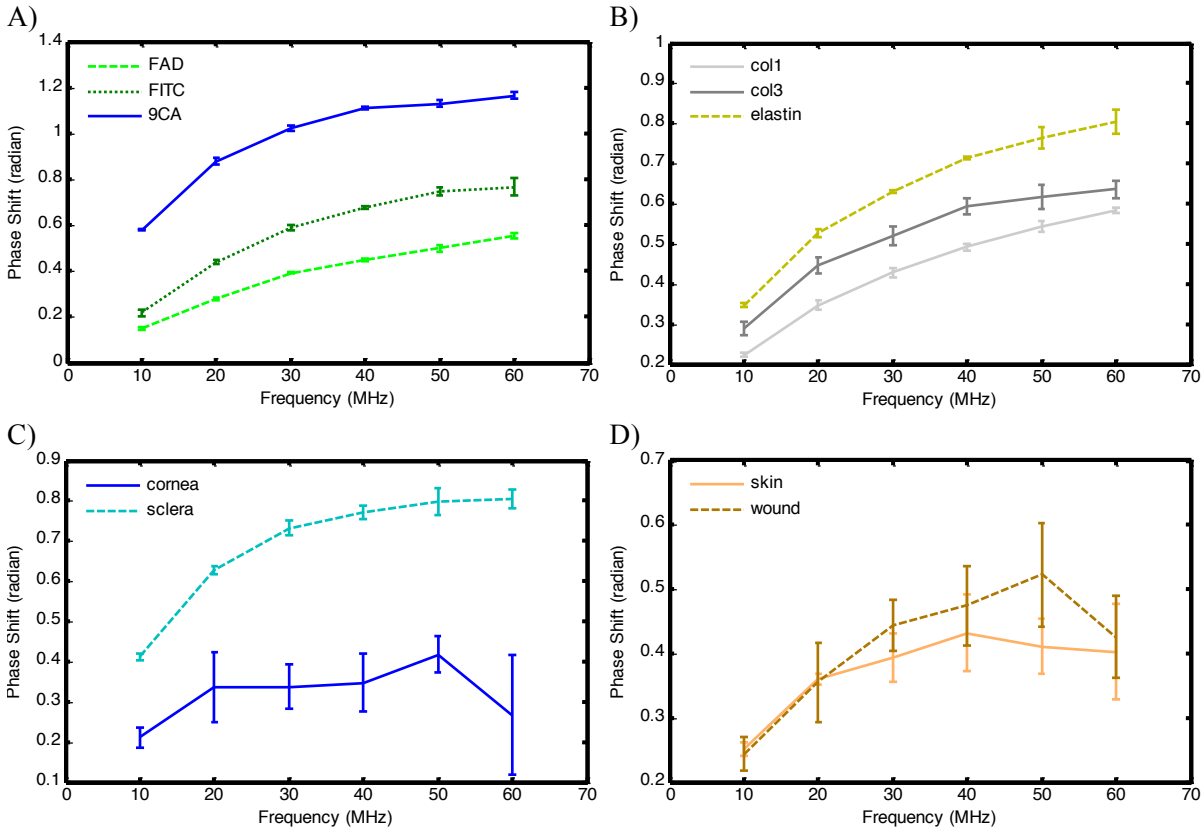


**Figure 5. Phase shifts are consistent with lifetimes of fluorescence standards and can distinguish ECM proteins that comprise tissues.** A) Fluorescence standards showed increasing phase shift between FAD, fluorescein, and 9CA, as expected by the order of their increasing lifetimes. B) Phase shift between type I and III collagen are distinct, and type III can be separated from elastin C) Ocular cornea tissues have smaller phase shift than sclera tissue, while D) wound tissues have larger shift compared to normal skin tissue. Error bars denote standard deviations, n=3.

### Frequency Domain Demodulation Results

Modulation depth ratios of the tested samples indicated that FD demodulation can distinguish collagen proteins that comprise tissues, Figure 6. The modulation depth ratios were seen to drop with frequency as expected, following a decay profile consistent with equation (8). At a particular frequency, deeper demodulation generally translates to longer lifetime. Modulation depth ratios from the standards followed that of the phase shift results, with FAD, fluorescein, and 9CA in the order of increasing lifetimes, Figure 6A. Again, collagen I versus III measured distinct modulation depth ratios, both shallower than elastin's values, Figure 6B. Ocular tissue demodulation also agreed with the phase results, with sclera having deeper demodulation and

thus longer lifetime than cornea tissue, Figure 6C. The murine wound also exhibited deeper demodulation compared to normal skin tissue, Figure 6D, consistent with the aforementioned premise that type III collagen is deposited into wound tissues during healing.

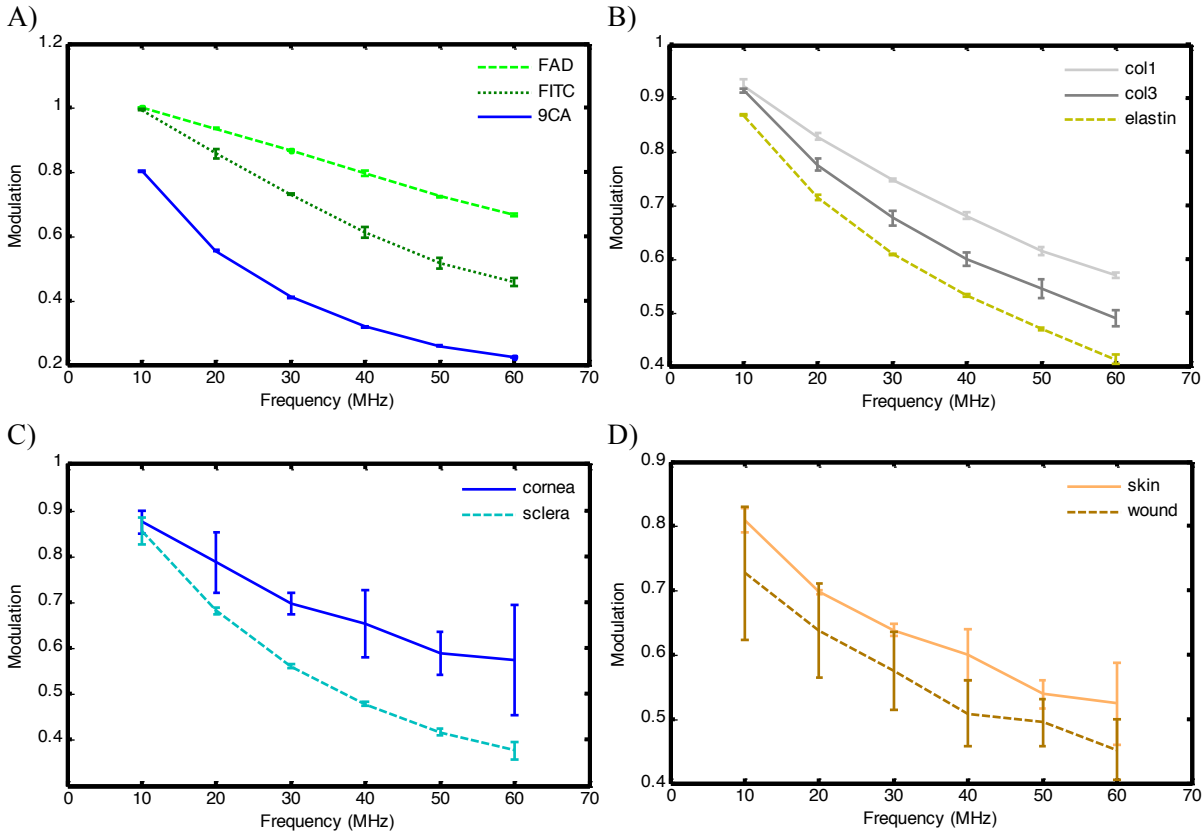


**Figure 6. Demodulation results can also distinguish collagen proteins that comprise tissues.** A) Fluorescence standards showed deeper demodulations between FAD, fluorescein, and 9CA, as expected in the order of their increasing lifetimes. B) Modulation depth ratios between type I and III collagen were distinct, and type III could be separated from elastin. C) Ocular cornea tissue had shallower apparent demodulation than sclera tissue, while wound tissue had marginally deeper demodulation compared to normal skin tissue. Error bars denote standard deviations, n=3.

Furthermore, the demodulation results also showed that the frequency band of 40-50 MHz has adequate separation for all samples. In the following section on the multi-exponential model, both the phase and demodulation results were combined in a minimizing function in order to calculate the combined lifetimes.

**Multi-exponential Fitting of Collagen, Elastin, and Tissue Lifetimes**

The phase shifts and modulation depth ratios were fitted into single or multi-exponential decay models, weighted with their respective standard deviations, by minimizing equation (9). The fitted lifetimes are shown in Tables 2-5. A single exponential model was used to fit for the fluorescent standards. The fitting showed results of 2.57, 3.94, and 11.75 ns for FAD, FITC, and 9CA, respectively, which are comparable to results in [21, 22, 27]. Protein samples were fitted to a two-exponential model, with a longer lifetime component and a shorter one around 1 ns, consistent with reported values [19, 20, 27]. Collagen III's average lifetime was measured at 5.01 ns, distinct from and longer than the lifetime of collagen I, 3.95 ns, p=0.001. Other reports have also found longer lifetimes for collagen III compared to I [17, 18]. This trend for collagen III vs. I has also been confirmed by using a time-domain system. Elastin was distinct from type III collagen, p=0.0002, and measured the longest average lifetime of ECM proteins in this study, with a value of 6.78 ns.

**Table 2. Single exponential fitting for fluorescence samples**

| sample | lifetimes (ns) | | pre-exponential factors | | fractional intensities | | average lifetime (ns) |
|---|---|---|---|---|---|---|---|
| | $\tau_1$ | $\tau_2$ | $\alpha_1$ | $\alpha_2$ | f1 | f2 | $\tau_{avg}$ |
| FAD | 2.57±0.02 | - | 1 | - | 1 | - | 2.57±0.02 |
| FITC | 3.94±0.05 | - | 1 | - | 1 | - | 3.94±0.05 |
| 9CA | 11.75±0.02 | - | 1 | - | 1 | - | 11.75±0.02 |

**Table 3. Multi-exponential fitting for protein samples**

| sample | lifetimes (ns) | | pre-exponential factors | | fractional intensities | | average lifetime (ns) |
|---|---|---|---|---|---|---|---|
| | $\tau_1$ | $\tau_2$ | $\alpha_1$ | $\alpha_2$ | f1 | f2 | $\tau_{avg}$ |
| col1 | 6.77±0.24 | 0.84±0.04 | 0.121 | 0.879 | 0.525 | 0.475 | 3.95±0.13 |
| col3 | 7.46±0.24 | 0.76±0.09 | 0.150 | 0.850 | 0.633 | 0.367 | 5.01±0.22 |
| elastin | 9.37±0.40 | 1.42±0.20 | 0.238 | 0.762 | 0.673 | 0.327 | 6.78±0.17 |

**Table 4. Multi-exponential fitting for ocular tissue samples**

| sample | Lifetimes (ns) | | Pre-exponential factors | | Fractional intensities | | Average lifetime (ns) |
|---|---|---|---|---|---|---|---|
| | τ1 | τ2 | α1 | α2 | f1 | f2 | τavg |
| cornea | 8.44±0.82 | 0.22±0.05 | 0.024 | 0.976 | 0.486 | 0.514 | 4.27±0.84 |
| sclera | 9.53±0.25 | 1.03±0.09 | 0.254 | 0.746 | 0.759 | 0.241 | 7.48±0.23 |

**Table 5. Multi-exponential fitting for wound skin samples**

| sample | Lifetimes (ns) | | Pre-exponential factors | | Fractional intensities | | Average lifetime (ns) |
|---|---|---|---|---|---|---|---|
| | τ1 | τ2 | α1 | α2 | f1 | f2 | τavg |
| skin | 13.08±0.80 | 0.72±0.14 | 0.049 | 0.951 | 0.484 | 0.516 | 6.72±0.24 |
| wound | 18.98±0.42 | 1.15±0.32 | 0.052 | 0.948 | 0.475 | 0.525 | 9.74±0.96 |

A two-exponential fitting was used for the tissue samples, follow by the calculation of τavg. For the ocular tissues, cornea measurements showed much shorter average lifetimes of 4.27 ns than sclera at 7.48 ns. For the murine skin tissues, the 8 mm murine skin wound at 14 days post-wounding showed a distinct, longer average lifetime at 9.74 ns versus normal skin at 6.72 ns. This is attributed to the bias of collagen III fibers (with longer lifetimes) laid down during the wound healing process. Murine wounds models used in this study have been reported [1] to express high level of type III collagen around 10-17 days post wounding, coinciding with the day 14 sample in the present study. It should be noted that tissue autofluorescence is comprised of numerous potential fluorophores other than collagen and elastin. The two-exponential fitting, while adequately describing the tissue measurements in this manuscript, could be improved by the addition of spectral-lifetime discrimination, as discussed in the Future Modifications section.

**Performance of FD ECM Detection System**

To provide a comparison of the temporal resolution and the sensitivity of the FD ECM

detection system, Figure 7 shows the standard deviations of repeat lifetime measurements of different sample amounts (collagen I mass and FAD concentration), which correspond to a range of emission intensities (Power). At lower mass/concentrations, FD lifetime measurements remain the same, but include greater standard deviations. A limit of 5% relative standard deviation was used, i.e. ~20 times signal to error ratio, as a cut-off for the limit of detection (LOD) determination. The sensitivity results showed that the system has a LOD of 25 µg for type I collagen and a LOD of 1 µM for FAD detections, while maintaining below 5% relative standard deviation. At both collagen and FAD LODs, the detected optical power was ~3 nW, corresponding to a time resolution of ~200 ps.

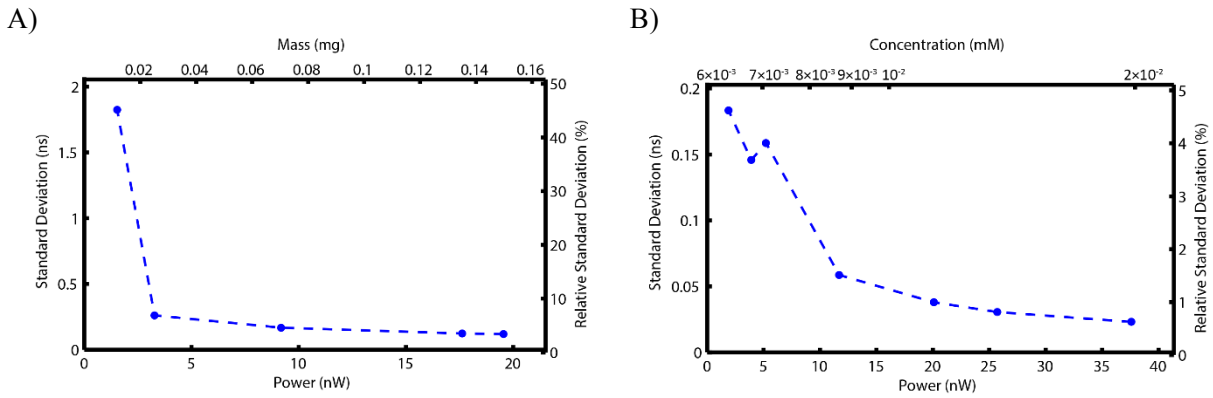


**Figure 7. FD ECM detection system sensitivity.** A) Limit of detection of solid samples was characterized by using collagen I detections at various masses, with the resultant time resolutions (in ns) and relative standard deviations plotted against power and mass. B) Limit of detection of liquid samples was characterized by using FAD detection at various concentrations, with the resultant time resolution and relative standard deviations plotted against power and concentration.

With respect to skin tissue detections, the probe illuminated a spot size of 5 mm, with penetration depth below ~300 µm (365 nm light). This geometry is equivalent to an excitation volume of 6 µL. Considering skin collagen composition to be ~70% by weight [30], in vivo measurements would involve ~4.1 mg of collagen using the probe. Therefore, FD ECM detection system provides two orders of magnitude finer sensitivity (25 µg vs. 4.1 mg) with

200 picosecond temporal resolution than required for tissue detection, adequate for resolving type I versus type III collagen in the skin.

**Future Modifications for Complex Tissue ECM Collagens**

Although the focus of the detection here is types I and III collagen, ECM compositions of tissue can involve a number of additional collagen types. In ocular tissue, fibrils are primarily composed of type I collagen, although types III, IV, V, VI, VIII, XII and XIII have also been identified to a lesser extent [25, 8]. In skin, collagen IV and VII are associated with basement membrane and dermoepidermal junctions. In addition to multiple collagen types, other ECM proteins like elastin and fibronectin create a complex detection mixture. First, future modification of the described detection system will include focusing on the frequency band of 40-50 MHz, which simplifies data acquisition and analysis without sacrificing collagen and elastin differentiation, as shown by the results given here. Next, instead of integrating all intensities above 400 nm, the emission can be divided into 400-450 nm, 450-500 nm, and 500-550 nm spectral bands using a simple filter wheel setup. These bands may reveal additional biases towards lifetimes of different collagen types and elastin. This should provide improved discrimination in a combined spectral-lifetime technique, as reported by others [31, 32], while still maintaining the simplicity of the LED-based FD ECM detection. Lastly, the multiexponential model could be adapted to predict the fractional contents of major fluorophores. For example, a four-exponential model with lifetimes of collagen I, III, elastin defined a priori, and a final residual exponential to account minor fluorophores, can be used to calculate the relative quantity of each defined protein. These future modifications should improve the discrimination of tissue autofluorescence and provide additional quantitative information on protein content without sacrificing system costs.

**Summary**

A low cost, low complexity, LED-based FD ECM detection system has been described and shown to be capable of measuring distinct lifetimes for type I and type III collagens and elastin. Fluorescence lifetimes of ECM proteins collagen I, III, and elastin were quantified with 0.2 ns resolution using the low-cost frequency domain method, to compare with the majority of time domain ECM measurements in the literature. The phase shift and modulation of the LED light source were calibrated at each scan frequency for both aqueous and solid samples. ECM protein samples were fitted to a two-exponential model, with type I collagen having shorter average lifetimes at 3.95 ns while type III at a longer 5.01 ns, distinct from the elastin lifetime at 6.78 ns. The probe was tested on bovine ocular tissues, with cornea showing much shorter average lifetimes of 4.27 ns than sclera at 7.48 ns. Furthermore, measurements of 8 mm murine skin wound at 14 days post-wounding also showed distinct, longer average lifetimes at 9.74 ns versus normal skin at 6.72 ns. Finally, the sensitivity results showed two orders of magnitude lower detection limits than typical tissue and skin collagen compositions, with 200 picosecond lifetime resolutions. Future modification of the FD collagen system will focus on the 40-50 MHz frequency range while separating the emission into three wavelength bands, providing additional spectral-lifetime discriminations. This work specifically targets and optimizes frequency domain lifetime detection of collagen variants in tissue, via a compact, easy-to-use package aimed at enabling clinical wound monitoring, tissue biomechanics monitoring, and other non-invasive biomedical applications. These results and the technique provide additional data points for collagen lifetimes in tissues, and further encourage clinical and interdisciplinary researches to use non-invasive optical biopsy for tissue monitoring.

**References**


1. J.R. Merkel, B.R. DiPaolo, G.G. Hallock, D.C. Rice. Type I and type III collagen content of healing wounds in fetal and adult rats. Proceedings of the Society of Experimental Biology and Medicine 1988;187:493-497.

2. P.G. Watson, R. Young. Scleral structure, organization, and disease. A review. Experimental Eye Research 2004;78:609-623.

3. R. Beuerman, A. Aplkama, J. Reynaud, N. Nguyen, H. Kikuchi, R. Kalia. Three-dimensional structure of the laminar cribrosa of the living eye. Proceedings of SPIE 2001;4431. doi:10.1117/12.447402.

4. M.J.A. Girard, A. Dahlmann-Noor, S. Rayapureddi, J.A. Bechara, B.M.E. Bertin, H. Jones, J. Albon, P.T. Khaw, C.R. Ethier. Quantitative mapping of scleral fiber orientation in normal rat eyes. Investigative Ophthalmology & Visual Science 2011;52(13):9684-9693.

5. T. Ihanamäki, L.J. Pelliniemi, E. Vuorio. Collagens and collagen-related matrix components in the human and mouse eye. Progress in Retinal and Eye Research 2004;23(4):403-434.

6. J.K. Pijanka, B. Coudrillier, K. Ziegler, T. Sorensen, K.M. Meek, T.D. Nguyen, H.A. Quigley, C. Boote. Quantitative mapping of collagen fiber orientation in non-glaucoma and glaucoma posterior human sclerae. Investigative Ophthalmology & Visual Science 2012;53(9):5258-5270.

7. R.A. Moses, J.W.J. Grodzki, B.C. Starcher, M.J. Galione. Elastin content of the scleral spur, trabecular mesh, and sclera. Investigative Ophthalmology & Visual Science 1978;17(8):817-818.

8. J.A. Rada, V.R. Achen, C.A. Perry, P.W. Fox. Proteoglycans in the human sclera. Evidence for the presence of aggrecan. Investigative Ophthalmology & Visual Science 1997;38(9):1740-1751.

9. Y. Komai, T. Ushiki. The three-dimensional organization of collagen fibrils in the human cornea and sclera. Investigative Ophthalmology & Visual Science 1991;32(8):2244-2258.

10. A. Thale, B. Tillmann, R. Rochels. Scanning electron-microscopic studies of the collagen architecture of the human sclera--normal and pathological findings. Ophthalmologica. 1996;210(3):137.

11. O. Schmut. The identification of type III collagen in calf and bovine cornea and sclera. Experimental Eye Research 1977;25(5):505-509.

12. R.E. Lee, P.F. Davison. The collagens of the developing bovine cornea. Experimental Eye Research 1984;39(5):639-652.

13. N.G. Strouthidis, M.J.A. Girard. Altering the way the optic nerve head responds to

intraocular pressure—a potential approach to glaucoma therapy. Current Opinion in Pharmacology 2013;13(1):83-89.

14. C.F. Burgoyne, D.J. Crawford, A.J. Bellezza, S.J.K. Francis, R.T. Hart. The optic nerve head as a biomechanical structure: a new paradigm for understanding the role of IOP-related stress and strain in the pathophysiology of glaucomatous optic nerve head damage. Progress in Retinal and Eye Research 2005;24(1):39-73.

15. E.J. Cohen, J.S. Myers. Keratoconus and normal-tension glaucoma: a study of the possible association with abnormal biomechanical properties as measured by corneal hysteresis. Cornea. 2010;29(9):955.

16. K. Trier. The Sclera. Advances in Organ Biology. Vol 10. Philadelphia: Elsevier BV; 2005:353-373.

17. P. Ashjian, A. Elbarbary, P. Zuk, D.A. Deugarte, P. Benhaim, L. Marcu, M.H. Hedrick. Noninvasive in situ evaluation of osteogenic differentiation by time-resolved laser-induced fluorescence spectroscopy. Tissue Engineering 2004;10(3-4):411-420.

18. L. Marcu, D. Cohen, J.M.I. Maarek, W.S. Grundfest. Characterization of type I, II, III, IV, and V collagens by time-resolved laser-induced fluorescence spectroscopy. Proc. SPIE 2000;3917. doi:10.1117/12.382720.

19. M.Y. Berezin, S. Achilefu. Fluorescence lifetime measurements and biological imaging. Chem. Rev. 2010;110(5):2641–2684.

20. J.E. Phipps, Y. Sun, M.C. Fishbein, L. Marcu. A fluorescence lifetime imaging classification method to investigate the collagen to lipid ratio in fibrous caps of atherosclerotic plaque. Lasers Surg. Med. 2012;44(7):564-571. doi: 10.1002/lsm.22059.

21. Y. Yuan, J. Hwang, M. Krishnamoorthy, K. Ye, Y. Zhang, J. Ning, R. C. Wang, M. J. Deen, Q. Fang. High-throughput acousto-optic-tunable-filter-based time-resolved fluorescence spectrometer for optical biopsy. Optics Letters 2009;34(7):1132-1134.

22. W.J. O'Hagan, M. McKenna, D.C. Sherrington, O.J. Rolinkski, D.J.S. Birch. MHz LED source for nanosecond fluorescence sensing, Meas. Sci. Technology 2002;13:84-91.

23. S. Fantini, B. Barbieri, M.A. Franceschini, E. Gratton. Frequency-domain spectroscopy, in: E. Kohen, J.G. Hirschberg, Applications of Optical Engineering to the Study of Cellular Pathology, Volume 2. Research Signpost, 1999, pp57-66.

24. P.G. Watson, B. Hazleman, P. McCluskey, C. Pavesio. The sclera and systemic disorders. 3rd ed. London: JP Medical, Ltd; 2012.

25. J.R. Lakowizc, G. Laczko, H. Cherek, E. Gratton, M. Limkeman. Analysis of fluorescence decay kinetics from variable-frequency phase shift and modulation data. Biophys. J. 1984;46:463-477.

26. Q. Fang, T. Papaioannou, J.A. Jo, R. Vaitha, K. Shastry, L. Marcu. Time-domain laser-induced fluorescence spectroscopy apparatus for clinical diagnostics. Review of

Scientific Instruments 2004;75(1):151-162.

27. T. Ihanamaki, L.J. Pelliniemi, E. Vuorio. Collagen and collagen-related matrix components in the human and mouse eye. Progress in Retinal and Eye Research 2004;23: 403-434.

28. G.E. Marshall, A.G.P. Konstas, W.R. Lee. Collagen in ocular tissues. British Journal of Ophthalmology 1993;77:515-524.

29. R.E. Neuman, M.A. Logan. The determination of collagen and elastin in tissues. Journal of Biological Chemistry 1950;186:549-556.

30. H. Xie, J. Bec, J. Liu, Y. Sun, M. Lam, D.R. Yankelevich, L. Marcu. Multispectral scanning time-resolved fluorescence spectroscopy (TRFS) technique for intravascular diagnosis. Biomedical Optics Express 2012;3(7):1521-1533.

31. D. Chorvat Jr., A. Chorvatova. Multi-wavelength fluorescence lifetime spectroscopy: a new approach to the study of endogenous fluorescence in living cells and tissues. Laser Physics Letters 2009;6(3):175-193.

# Chapter 3 3D Printed Miniaturized Spectral System for Collagen Fluorescence Lifetime Measurements

## Introduction

### Collagen spectral lifetime

Autofluorescence from collagen is commonly observed in fluorescence microscopy. The primary fluorophores contributing to collagen's fluorescence are pyridinium, tyrosine, and phenylalanine groups [7-10], which can be affected by crosslinking, glycation, and their compositions in different types of collagens [11-13]. The effects of these multiple fluorophores can be seen in the lifetime of the collagen fluorescence, with evidence that lifetimes also vary across the emission spectrum [14-16]. Spectral-lifetime detection, then, can help distinguish the compositions of collagen types in a mixed environment like tissue or the skin. A simplified model of spectral-lifetime fluorescence can be described by

$$\mathrm{I}(\lambda, t) = \sum_{i=1} \alpha_i(\lambda) e^{-t/\tau_i} \qquad (1)$$

Where the values of $\alpha_i(\lambda)$ represent the relative contribution of the $i^{th}$ fluorophore at wavelength $\lambda$. The frequency response is typically measured at several wavelengths resulting in wavelength-dependent phase angle and the modulation values [17].

We observed that under the same illumination, collagens have varying fluorescence lifetimes corresponding to different wavelength bands [3]. We hypothesize that under these conditions, there will be certain wavelength bands that augment the fluorescence lifetime separation of different collagens. To investigate this possibility, we divided the fluorescence emission into three channels using three dichroics at 387 nm, 409, and 435 nm. For wound healing

applications, tissue collagen composition changes from type III to type I. The aforementioned bands cover the peak, shoulder, and tail portion of the collagen autofluorescence.

**Optomechanics rapid prototyping via additive manufacturing**

Additive manufacturing has been widely popularized for rapid prototyping in recent works, including 3D printed optical systems. Despite the limited spatial resolution and plastic built material in current commercial printers, there are already efforts in testing and characterizing 3D printing for optical systems and optomechanical components [18]. Other optics and photonics applications include structured 3D phantoms [19], optofluidics [20], as well as miniaturized microscopy [21], in addition to numerous bioengineering applications. However, a high resolution printer is necessary in our microoptics design, where half inch optics need to be precisely aligned in a miniaturized setup. A 1º change in the dichoric orientation, for example, would incur a focal change on the order of 400 μm, which is a significant portion of the 1.5 mm diameter photodiode used in this microoptic system. To address this, a DLP (digital light processing) based lithography 3D printer with 43 μm resolution is employed to prototype the microoptics. DLP lithography is a 3D printing method that uses an ultraviolet light to photo-crosslink a liquid polymer substrate [22]. Models built with CAD drawing program can be easily inserted into the software for the 3D printer. This compact professional printer can give us 585 dpi print resolution, or 43 μm resolution, with a layer thickness of 30 μm. Unlike extrusion based method where models are printed line by line, DLP 3D printing is imaged layer by layer, and the resolution does not affect the print speed. Only several hours of printing, without machining, are required to prototype our device with complex internal structure within those geometric accuracies.

**System setup**

Motivated by the benefits and limitation of novel non-invasive techniques, we designed a compact, low-cost optical system based on frequency domain fluorescence lifetimes to measure tissue collagen, Figure 8. Three-dimensional (3D) printing was employed to prototype such miniature optical systems, while the optical components including dichroic, lenses, and filters were selected with a diameter of 0.5", creating an overall cylindrical device dimension of approximately 1.5" by 3". Thermal and mechanical characteristics of the 3D printed optomechanics were analyzed using finite element analysis (FEA) and found to have minimal effects on ray tracing. Sine-modulated excitation and spectrally separated frequency domain emissions were then digitized and analyzed in MATLAB to calculate their lifetimes. Our results showed that such compact, spectral-lifetime detection system balances the portability with specificity for differentiating collagen types, in a package that is suitable for tissue monitoring applications.

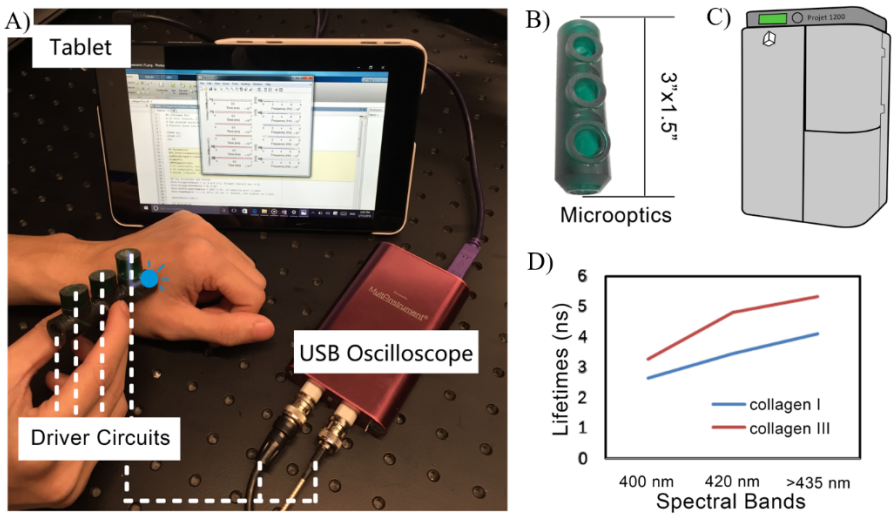


**Figure 8. Schematics of the 3D printed probe for tissue collagen differentiation.** A) The prototype system is comprised of the microoptics sytem, LED, photodiode, driver electronics, USB oscilloscope, and a tablet for data analysis. It is designed to measure tissue collagen compositions via frequency domain fluorescence detections. B) A 3"x1.5" prototype microoptics mount was enabled by C) 3D stereolithogrpahy printing with <50 µm resolution. D) By leveraging both spectral and lifetime spectroscopy, the prototype can provide better differentiation of the different types of collagen, e.g. I and III.

## Method

### Miniaturized optics

The system was based on free space optics with a common optical path for the excitation and the emission intensities to optimize coupling and increase signal, Figure 9. It achieved spectral lifetime measurements by breaking up incoming intensity into three different bands via a series of longpass dichroics. Specifically, the bands were separated by longpass dichorics at 387 nm, 409 nm and 435 nm. The first two bands, referred to here on as the 400 and 420 nm bands at their center wavelengths, correlated to the fluorescence emission profiles of collagens I and III. Wavelength above 435 nm, referred to here on as >435 nm band, can help to remove non-collagen backgrounds.

First, the modulated LED light source was filtered by a 357 nm, 44 nm bandpass filter and collected by an aspherical condenser lens to couple light towards the top surface of the first dichroic (387 nm, longpass). The 357 nm light was then reflected by dichroic, towards the lens at the sample. This excitation was illuminated on a fluorescence sample at a fixed geometry dictated by the 3D printed cavity and the lens' focal length. The resultant emission and scattering were collected reversely through the same lens geometry, and filtered through the same dichroic, removing non-fluorescent scattering below 387 nm. Similar to aforementioned LED/first dichroic stage, the emission light was directed onto two other dichroics at the prescribed longpass wavelengths. Each of the subsequent three wavelength bands was then focused by an aspherical condenser lens onto a fast, PIN photodiode. The complete list of optical and electronic components is described in Table 6.

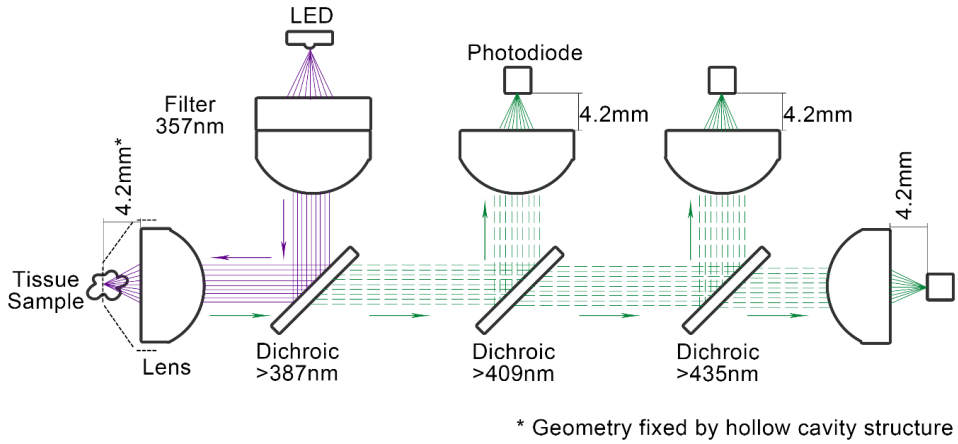


**Figure 9. Spectral lifetime microoptics system setup.** Three 45° longpass dichorics at 387, 409, and 435 nm separate the system into four stages. All lenses were designed as f 4.2 mm condenser lenses to simplify the design. The first stage filters and collimates the 357 nm LED light onto the dichroic and subsequently focuses it on a fluorescence sample, e.g. skin, at a fixed geometry described by the lens' focal length and a cavity within the 3D printed mount. Emission and scattering are collected through the same exact optical axis to maximize coupling, while the 387 nm dichroic removes the scattering intensities.

**Table 6. Component list of the system**

| Components | Type | Part | Specfications | Diameter | Volt | Price ($) |
|---|---|---|---|---|---|---|
| Sample Optical Coupling Lenses | Condenser | ACL108 | f 4.2 mm | 10 mm | | 16.8 |
| Excitation Optoelectronics | LED | Digikey 537-1092 | λ 365 nm | 4.4 mm | 4.1 V | 35.75 |
| Lenses | Condenser | ACL108 | f 4.2 mm | 10 mm | | 16.8 |
| Filter | Band pass | Edmund 86-973 | λ 357 nm | 12.5 mm | | 180 |
| Dichroic | Longpass | Chroma T387lp | λ 387 nm | 12.5 mm | | 300 |
| 400 nm Band Optoelectronics | Photodiode | Thor FDS025 | λ 400-1100 nm | 5.4 mm | 20V | 30 |
| Lenses | Condenser | ACL108 | f 4.2 mm | 10 mm | | 16.8 |
| Dichroic | Longpass | Edmund 86-309 | λ 409 nm | 12.5 mm | | 140 |
| 420 nm Band Optoelectronics | Photodiode | Thor FDS025 | λ 400-1100 nm | 5.4 mm | 20V | 30 |
| Lenses | Condenser | ACL108 | f 4.2 mm | 10 mm | | 16.8 |
| Dichroic | Longpass | Edmund 87-051 | λ 435 nm | 12.5 mm | | 140 |
| >435 nm Band | | | | | | |

| | | | | | | |
|---|---|---|---|---|---|---|
| Optoelectronics | Photodiode | Thor FDS025 | λ 400-1100 nm | 5.4 mm | 20V | 30 |
| Lenses | Condenser | ACL108 | f 4.2 mm | 10 mm | | 16.8 |
| Digitization | | | | | | |
| Computer | Tablet | Dell Venue 8 Pro | Matlab | 8” | 5V | 250 |
| Oscilloscope | USB | Virtins 2820R | 200 MHz | | 5V | 250 |

**Custom built optomechanics**

To house the optical system, a tube was designed as two halves split down the center of its vertical orientation, with several joints added on to provide the mating surface, Figure 10A. The three dichroics dividing the system into four stages were designed with minimal distance from each other, allowing several millimeters for LED, heatsink, PIN photodiode alignment and mounting only. The shorter component distances, common axis, and free space design of the microoptics system ensures minimal coupling loss in a miniaturized package.

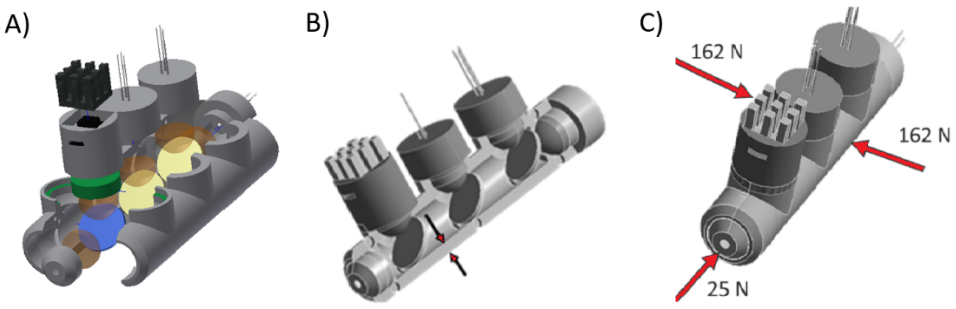


**Figure 10. 3D optomechanics system and FEA parameters.** A) The grey components represent the optical tube mounts and LED/photodiode adapters that were 3d printed. The blue and gold colored filters represent the ½” longpass dichroics at prescribed wavelengths. The transparent orange shapes are 10 mm condenser lenses to provide the focusing and collimation for each stage. The overall dimension of the tube, not including the adapters, is around 1.5” x 3”. B) Device thickness was varied in simulation. C) Mechanical loading on device was modeled after normal gripping (162 N) and adequate contact on sample/skin (25 N).

The coupling of the system can be interpreted by the optical power measured at various stages in the microoptics system. A cellulose-based paper business card, was used for coupling measurements due to its similarity in excitation/emission wavelengths as collagen and its

strong fluorescence, Table 7. The power of the LED module going into the optics and the resultant power at the sample plane were measured as I0 and Icoupled, respectively, for the excitation stage. The resultant fluorescence from the paper was then measured with a calibrated spectrometer at their appropriate wavelengths. The Icoupled for each of those bands are then measured after the appropriate dichroics and lenses, at their respective photodiode positions.

**Table 7. Measured coupling at different stages of the microoptics system**

| Stages | | I0 (**µW**) | ICoupled (**µW**) |
|---|---|---|---|
| Excitation | | 19.9 | 16.2 |
| Paper* | 400 nm | 0.16 | 0.06 |
| | 420 nm | 0.12 | 0.05 |
| | >430 nm | 0.11 | 0.90 |

*Paper as a fluorescent sample, 350 mA amplitude LED excitation.

**Thermal and mechanical FEA**

The design of the 3D printed optomechanic system was evaluated by both thermal and mechanical analyses using a 3D CAD model of the device and FEA. Initially, a 3D model of the microoptics system was constructed in CAD software (Inventor, Autodesk Inc.). The model was then discretized into a mesh geometry that was constrained and joined by nodes. The mesh model was then applied in the thermal and mechanical analyses with appropriate governing equations. Three-dimensional thermal strain was computed by specifying the thermal properties of the material (such as specific heat, thermal conductivity, etc.) and applied conditions (such as heat flux, temperature boundary conditions, etc.). In addition to stress and strain, the 3D temperature distribution was also obtained. FEA for both transient thermal and steady state thermal analyses were conducted using ANSYS. Similar to the thermal analysis, external mechanical loads from device handling were applied to the discretized finite element mesh in combination with defined material properties, to allow for numerical determination of strain at each elemental node and the stresses within each element. The deformations

subsequent to both thermal and applied mechanical loading were determined for several combinations of structural and material considerations.

**FEA parameters investigated**

The primary heating load for the device came from the LED that generated the incident light prior to contacting the tissue. The LED was obtained from Digikey (537-1092-1-ND) capable of 1 A current at 4.1 V. Based on our system coupling characterizations and typical tissue fluorescence emission, Table 7, we designed the LED with a maximum modulation of 200 mA to maintain photodiode intensities around a fraction of μW. Since current LED efficiency peaked at 40 % especially for blue wavelengths [22, 23], the joule heating was estimated at 0.5 W. Thus the analysis was carried out by applying a heating load of 0.5 W to all surfaces directly exposed to the LED. Various structural thicknesses were investigated using this thermal modeling, Figure 10B.

Contrary to the single thermal load, the detection system was subject to multiple mechanical loads. The device is to be held by a clinician, which is translated into two forces applied perpendicularly to both sides of the device. Based on studies of hand-held device in "Key Pinch" positions [24], right handed males at 20-24 years of age had an average key pinch strength of 36.5 lbf or 162 N (90th percentile of this demographic). Thus, we simulated a load of 162 N to both sides of the device, Figure 10C. Additionally, the device was designed to come into contact with the patient's body during normal operation. Therefore, it was assumed that the frontal load on the device would be no more than 15 % of the gripping strength, or 25 N applied at the front of the device, Figure 10C. Various thicknesses were investigated using this mechanical loading model.

Our stereolithography technique is limited by its print material, unlike the array of available plastics in extrusion based 3D printing techniques. To investigate whether material choice is a factor in our printed geometry, we simulated the structure using three different materials—VisiJet® FTX Green, Polylactic Acid (PLA) and Acrylonitrile Butadiene Styrene (ABS). VisiJet is the material used in our stereolithography printer, while PLA and ABS are available in extrusion based 3D printers. Along with the variation of the material type, four wall thicknesses—2.54 mm, 3.175 mm, 3.81 mm, and 4.45 mm (0.1", 0.125", 1.5", & 1.75")—were also investigated to determine the optimal dimension for each material.

**Optical ray tracing**

Ray tracing program TracePro (Lambda Research) was used to model the light propagation in the device and demonstrate the feasibility of optical system. This was done on a geometry with the optimal wall thickness as characterized from the thermal and mechanical FEAs. Due to the common path of the fluorescence excitation and emission employed in this design, the ray tracing was broken into two parts—excitation and emission geometries. Only the geometric optics without scattering or multiple reflections were modeled. Four wavelengths—one excitation and three for each emission bands—were simulated separately in the ray tracing. The positions of the optics and the optimal material thickness from FEA were adjusted to optimize the ray tracing towards the smallest spot sizes to ensure maximum coupling.

**Frequency domain method**

The prototype was applied to the detection of collagen I and III samples (dried fiber from bovine origin obtained from Sigma Aldrich, catalogue numbers C9879-1G and CC078 for type I and III, respectively). During data acquisition, the raw emission signals from the photodiodes were digitized by the USB oscilloscope. To remove nonlinear DC offsets from different scaling

and frequencies of the raw signals, offsets from dark readings (LED turned off) at specific measurement conditions were subtracted from the raw data before fitting and data processing. This process allowed more accurate calculations of the phase shift angles and modulation depths, without peak uncertainties, amplitude drifts, and waveform asymmetries from one part of the raw data to another. Raw data of 2x104 points were acquired by the oscilloscope, segmented into 1250 points strings, and averaged together to provide a working data length. This self-averaging allowed for faster data acquisition while averaging over data jitters. FFT was done on this data length to extract the phase and modulation components at the particular frequency that was scanned. Frequencies at 10, 20, 30, 40, 50, and 60 MHz were scanned, and ten sets of frequency scans were done for each sample being measured. All of the data acquisition and signal analysis were done within Matlab (Mathworks, Inc.) with vendor supplied hardware drivers.

After calculating the phase angles and modulation depth ratios between 10 MHz and 60 MHz, the data was fitted to a multi-exponential model [6, 25], where the fluorescence impulse response function was described in equation (1). Thus, the fractional intensity observed in the usual steady-state measurement due to each component in the multi-exponential decay [17] is

$$f = \frac{\alpha_i \tau_i}{\sum_j \alpha_j \tau_j} \quad (4)$$

Where $\sum f_i = 1$. Lifetime can be finally calculated by

$$\tau = \sum f_i \tau_i \quad (5)$$

**Electronics and data acquisition**

The optoelectronics and data acquisition of the system were designed to achieve optimal portability. A custom LED driver circuit and switchable photodiode transimpedance amplifier were initially designed for the microoptics system. However, both prototype boards were too

large at 1”x3” dimensions and not suitable for integration. Therefore, the biophotonics results were finally obtained by guiding an LED source modulated at 10-60 MHz (Thorlabs DC3100-365) to the microoptics system via a 0.22 NA 600 μm UV solarized fiber cable (Stellarnet). Similarly, the emissions after each dichroic were manually guided to an avalanche photodiode (Thorlabs APD120A2) with 2.5 x 106 V/W gain via 600 μm fiberoptics.

Digitization of both the LED trigger signal and photodiode signal was provided by USB DSO (Virtins DSO-2820R). 2x104 sample data at 2 GS/s were acquired within the DSO’s software. Raw data were imported into Matlab for FFT analysis and calculation of the fitted two exponential decay models as described earlier. All computer controls were performed on a Dell Venue 8 Pro tablet running Windows 10. The entire portable package, include the computing unit, battery, and microoptics, weighed less than 4 pounds and can fit in a small suitcase, Figure 8.

**Result and discussion**

Thermal and mechanical FEA were conducted before the devices was printed. Both models showed negligible deformations which did not lead to loss of optical performance. The geometry was further optimized with ray tracing to form the final 3D printed structure. After calibration of the devices, lifetimes of type I and III collagen in the three wavelength bands were measured and calculated.

**Thermal FEA results indicate negligible strain**

As stated earlier, the thermal analysis was carried out with the assumption that all surfaces exposed to the LED underwent a heat flow of 0.5 W. All temperature gradients were localized near the LED emitter, as the plastic material are expected to have low thermal conductivity. A

temperature probe was placed on the cylinder surface below the LED emitter and its readings were plotted for the different materials in Figure 11A. During our modeling, temperature distributions remained within 2.54 mm of the wall thickness. Thus, thermal analyses were only carried out at a wall thickness of 2.54 mm for each material.

A clear difference in the materials' response to the heating load can be observed. Over a period of 60 seconds, VisiJet® FTX Green was clearly the superior choice in terms of heat dissipation. Furthermore, ABS was the most inferior material with respect to thermal performance, reaching a temperature over 110°C after 60s. The device is expected to be operated in short measurement durations, e.g. several seconds each for the three channels and dark noise readings, totaling up to ten second or so of continuous operation. At these conditions, the PLA and VisiJet temperatures stayed below the typical scalding temperatures for contact, which would be reached at 60°C after 20s. Thus, by considering only the thermal characteristics, it is evident that PLA and VisiJet® FTX Green were comparable options for the device's structural material. It should be noted that all materials showed negligible thermal strain for their respective maximum temperatures reached. Therefore, the thermal characteristics of various materials was only considered from an operator's safety and comfort perspective rather than the functional optomechanics perspective.

**Mechanical FEA results are comparable to other 3D printings**

On the other hand, the device was subject to the mechanical loading conditions described in the FEA parameters section. The device experienced deformation along multiple axes during the simulation. However, only the deformation that occurred normal to the main optical axis of device appeared to be significant. Deformation along other axes of the device were minute and evenly distributed, so any lateral distortions to the optical mounts and dichroic were

negligible. To compare the various materials, the maximum interior deformations of the device were plotted for various wall thicknesses in Figure 11B. All three materials observed the same amount of deformation for wall thicknesses of 2.54 mm and 3.175 mm. When the wall thickness increased beyond 3.175 mm, a noticeable difference across the various materials occurred. Notably, all materials had deformation that leveled out at thickness above 3.81 mm. Based on lowest stress-strain curve, PLA was the ideal choice for the structural components, followed by ABS and then VisiJet® FTX Green. In addition, 3.81 mm was the optimal thickness for PLA and ABS, while no improvements were observed for VisiJet with thickness above 3.175 mm for the designed optomechanics geometry. Post FEA, all subsequent designs and builds using our Projet 1200 stereolithography printer adopted a 3.175 mm thickness.

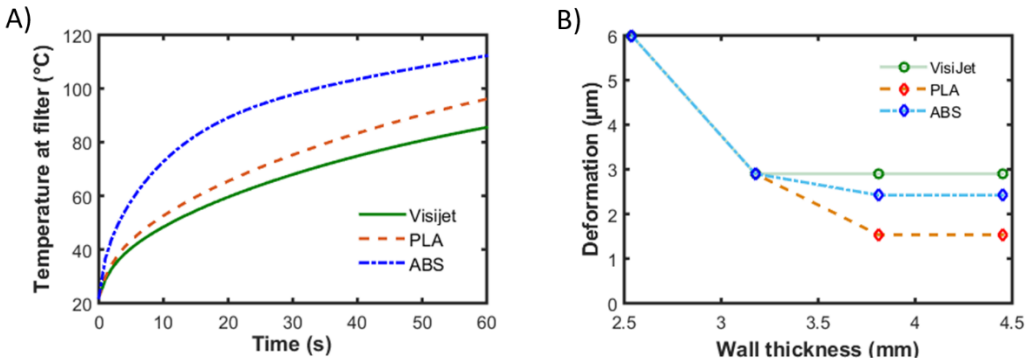


**Figure 11. Thermal and mechanical FEA for wall thickness and materials in 3D printing.** To compare the materials between stereolithography and extrusion based 3D printing, ABS, PLA, and VisiJet Green (3D Systems) were investigated for thermal distribution and mechanical deformation in the designed geometry. A) Temperature gradient localized around the LED emitter showed that ABS developed higher temperatures than PLA or VisiJet Green. Temperature measured in VisiJet material remained below 60°C after 20s of typical LED operation. B) Maximum deformation inside the microoptics housing is plotted at different wall thicknesses for the three printing materials. All materials have similar deformations below 3.175 mm, while ABS maintains the lowest deformation at higher wall thicknesses.

### Ray tracing for optical optimization

At the optimal wall thickness modeled in the thermal and structural analyses of the photonic reader device, there was no observable effects upon the ray tracing performance of the device.

The deformations of the housing and the subsequent relative motions of the optical components still resulted in appropriate optical quality and performance, as simulated through the optical ray tracing. Furthermore, to ensure minimal coupling losses, the distances between parts were optimized to produce ray tracing with the smallest spot sizes.

Ray tracing of the excitation stage was modeled separately from the rest of the system to simplify the common axis for fluorescence in the optomechanical design, Figure 12A. 365 nm light from the LED passed through an excitation filter and a condenser lens, reflected from a 45 ° dichroic, and was focused on a sample through a second condenser lens. Due to the finite size of the LED emitter (2.3 mm), its image at the sample was adjusted relative to the focal length of the condenser lens in order to achieve a focused spot of 2.6 mm, Figure 12B.

Next, the emission stages corresponding to the three detection bands were modeled in ray tracing using 400 nm, 420 nm, and 435 nm wavelengths, Figure 13A. The resultant intensity showed spot sizes of 1.8, 1.5, and 1.5 mm diameters at the detector planes of the 400 nm, 420 nm, and >435 nm stages, respectively, Figure 13B. After the ray tracing analysis, the CAD design was updated for 3D printing. The final 3D printed geometry represented the optimized structure that provided the smallest spot size via ray tracing.

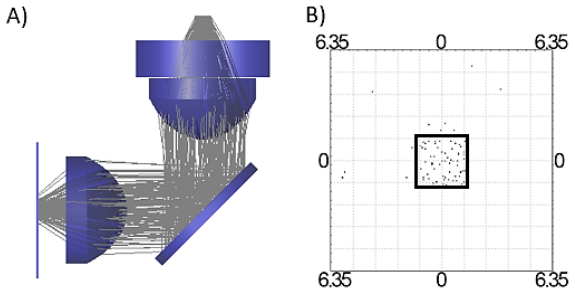


**Figure 12. Optical ray tracing simulation of the excitation stage.** Excitation ray tracing is simulated from the LED source through filter, lenses, dicroic, and finally the sample. A) profile view of the ray tracing for the excitation stage. B) Total irradiance map on the surface of sample. The light spot is around 2.6 mm by 2.6 mm, which is close to the size of LED light source of 2.3 mm, represented by the square box.

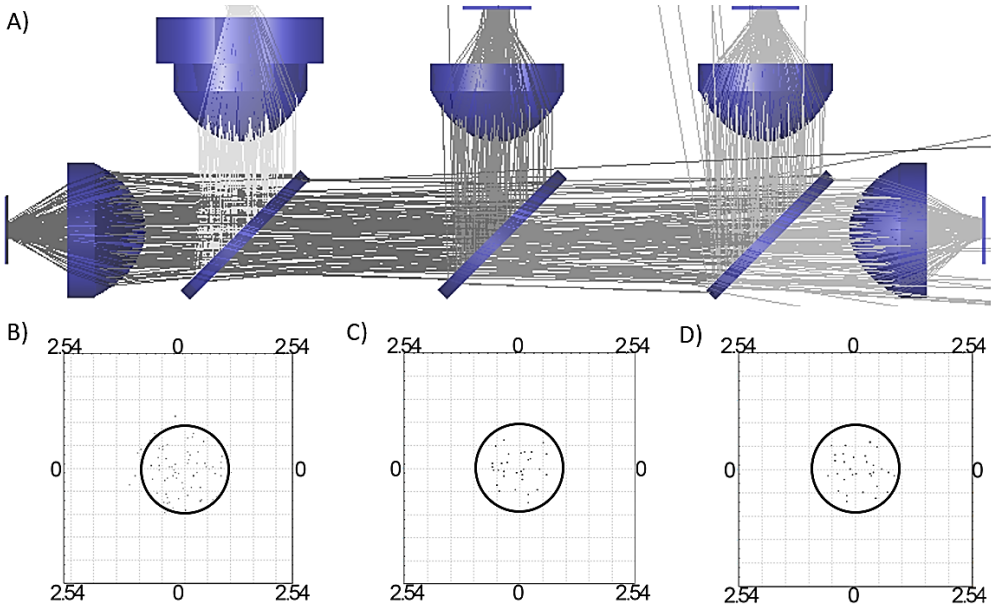


**Figure 13. Optical ray tracing simulation of the emission stages.** Emission ray tracing is simulated from the sample, through the optical system and to target photodiodes for each detection band. A) profile of ray tracing with the diameter of fluorescence light source at 2.6 mm. B), C) and D) represent the total radiance on photodiodes, which have size of 1.8, 1.5, and 1.5 mm, respectively. The circles provide references to the actual photodiode sensor area.

### Frequency domain phase shift results

For both collagen samples measured, the phase shift angles rose with increasing frequency with an inverse tangent profile, Figure 14A, B, consistent with equation (2). Higher phase shift denotes to longer lifetime at a particular frequency. Upon closer examination of the differences between the three channels, the first channel always resulted in the lowest phase shift. At higher frequencies, 420 nm band phase shift rose above that of the >435 nm band for collagen I, but the two bands overlapped across frequencies for collagen type III.

### Frequency domain demodulation results

For both collagen samples measured, the modulation depth ratios decreased with increasing frequency following a decay profile, Figure 14C, D, which was consistent with equation (3). At a particular frequency, deeper demodulation generally denotes longer lifetime. As a trend,

collagen I had shallower demodulation than collagen III. Specifically, modulation depth ratios showed more separation between 400 nm and 435 nm bands, as the measurements showed consistent, smaller standard deviations.

**Frequency domain lifetime**

To differentiate the lifetimes of type I versus type III collagen for the three spectral channels, phase and demodulation data were fitted in a two-exponential decay model and tabulated in Table 3. In the table, τφ is the phase shift lifetime, τm is the demodulation lifetime, and τ is the apparent lifetime. Apparent lifetimes were calculated using a minimization function that weighed both phase and demodulation data according to their standard deviations. Spectral lifetime results in Table 8, which ranged between 2-4 ns for type I and 3-5 ns for type III, compared well with lifetime measurements from other collagen autofluorescence reports [4-6, 26, 27].

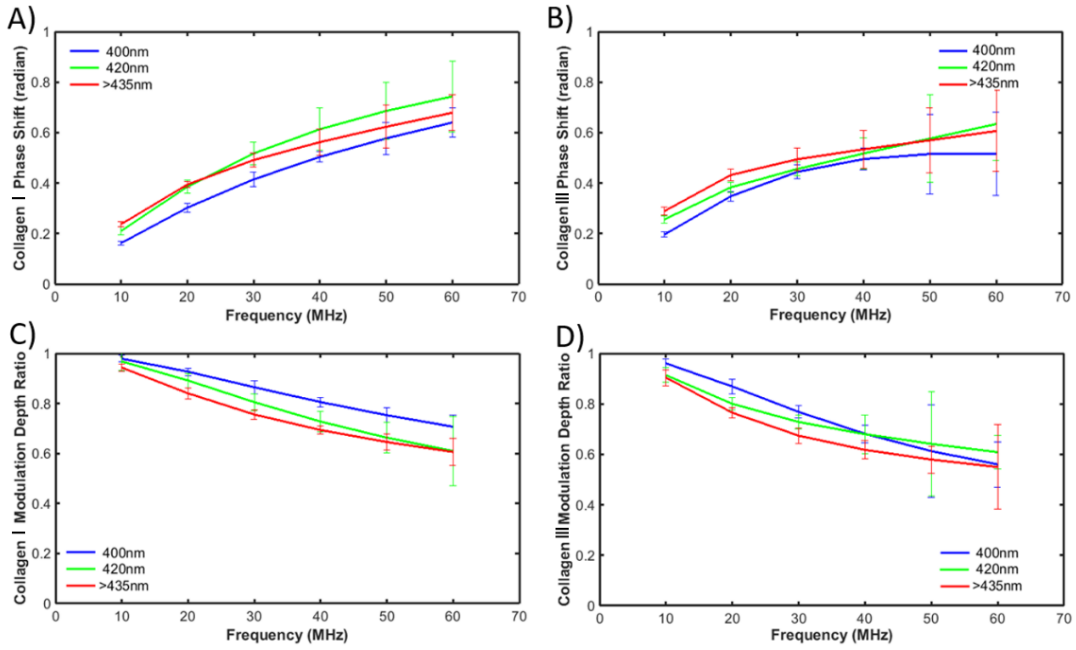


**Figure 14. Frequency domain results for spectral-fluorescence separation of collagen I/III.** Collagen I results are shown in the left hand column (A and C), while collagen III results are shown in the right (B and D). For both the phase (top row) and modulation (bottom row) graphs,

the 400 nm, 420 nm, and >435 nm bands are plotted as blue, green, and red, respectively. 400 nm bands showed phase and modulation results consistent with shorter lifetimes for both types of collagen. Phase results for collagen I, A), are smaller than that of collagen III, B), but collagen III flattens out above 30 MHz. Similarly, modulation results for collagen I, C), are shallower than that of collagen III, D). Generally, bands for collagen type I are further separated, while collagen type III has more overlaps and crossovers.

**Table 8. Calculated lifetimes for collagen I and III at multiple bands**

| Type | Lifetime | 400 nm | 420 nm | >435 nm |
|---|---|---|---|---|
| Col I | $\tau_{\varphi}(ns)$ | 2.2767±0.0442 | 2.9151±0.0516 | 2.8211±0.0430 |
| | $\tau_{m}(ns)$ | 3.0007±0.1769 | 3.8135±0.2552 | 4.4541±0.0955 |
| | $\tau(ns)$* | 2.6484±0.0599 | 3.4559±0.1116 | 4.1087±0.1310 |
| Col III | $\tau_{\varphi}(ns)$ | 2.3380±0.0926 | 2.7091±0.1024 | 2.9145±0.0544 |
| | $\tau_{m}(ns)$ | 4.3116±0.3625 | 4.9300±0.1649 | 5.6041±0.1655 |
| | $\tau(ns)$* | 3.2600±0.1462 | 4.8088±0.1954 | 5.3316±0.1626 |

*Apparent lifetimes via two-exponential fitting.

Time domain (TD) references provided for comparison.

Lifetimes increased from 400 nm, to 420 nm and above 435 nm for both collagens. Collagen III had longer lifetime than collagen I. In our results, both spectral intensities and lifetimes contribute to the separation of the collagen I versus III. 400 nm band had higher signal intensities in general, but smaller lifetime differences between the collagen types, while 420 nm band had lower signal intensities but greater lifetime differences. In the application of wound healing monitoring, where closed wound undergoes collagen remodeling from type III to type I collagen [1, 2], the emission intensity will be reduced, and 400 nm band should provide an important measurement due to its higher intensity. However, 420 nm band should provide a better lifetime contrast despite its lower intensity. By leveraging both channels for spectral-lifetime detection, more precise differentiation, and thus accurate monitoring of tissue collagen can be achieved.

**Future works**

Despite efforts to miniaturize the optomechanics structure, the prototype LED driver and photodiode transimpedance amplifier circuitry still required significant space. Additional embedded solutions are needed to provide further electronics integration. Moreover, data acquisition was done manually with DSO's software and imported into Matlab. A simple graphical user interface should make system operation user-friendly and less prone to errors. Additional structural mechanics such as the handle housing and wiring have yet to be implemented as well. The low intensity in actual tissue applications may require the use of avalanche photodiodes, which require higher bias voltages. Finally, multiple excitation wavelengths may be possible in the same optical train by the use of multi-colored LED diodes, which may broaden the available tissue fluorophores to detect, e.g. nicotinamide adenine dinucleotide (NADH).

The collagens used in this manuscript are purified fibrous proteins and intended as a proof of concept of the miniaturized probe. We have noticed different sources of proteins, e.g. skin, tendon, as well as different preparations and solutions greatly affect collagen autofluorescence lifetimes [5, 6, 27, 28]. An extensive tissue based study is necessary to provide confidence in the frequency-domain technique as a diagnostic tool, similar to efforts in time-domain studies [28]. In clinical applications, we envision the probe to be calibrated for individual patient's baselines, for example a person's normal skin versus healing wound. The relative differences of tissue collagens for that patient will then be the measurement instead of an absolute lifetime value, where the dynamics of the measurements over time provide diagnostic information rather than static snapshots.

In this study, the miniature spectra-lifetime system was applied to the detection of type I versus III collagen, which are the major parameters of tissue remodeling in a closed wound. In the

future, such portable spectral-lifetime system can be applied to clinical detection of advanced glycation end-products in diabetic skin, tissue fibrosis and scarring in wounds, and collagen/elastin compositions in aging skin, among others.

**Summary**

A miniaturized optical system was designed for spectral-lifetime measurements of collagens I and III. The system was comprised of a small tablet and USB DSO, LED, photodiode elements, and a 3D printed optomechanic structure, well-suited to portable detection applications. Thermal and mechanical FEA demonstrated negligible deformations during expected operation and handling of the device. Ray tracing further optimized the 3D printed optomechanics structure. Type I and III collagen lifetimes were measured across three spectral bands with our device, and were distinguished from each other. We found that 400 nm band gave higher signal intensity while the 420 nm band provided greater lifetime differences between collagen I and III. In tissue applications where low autofluorescence is combined with minute differences in collagen composition, multiple spectral channels with lifetime measurements may allow better collagen detections than either one along. The 3D prototyped miniature system has the potential to provide clinicians with a useful yet simple to use device for tissue collagen detections.

**References**


1. H.P. Ehrlich. The role of connective tissue matrix in wound healing. Prog. Clin. Biol. Res. 1988; 266:243–258.

2. M.J. Ranzer, L. Chen, L.A. DiPietro. Fibroblast function and wound breaking strength are impaired by acute ethanol intoxication. Alcohol Clin. Exp. Res. 2011; 35:83-90.

3. J.F. Almine, S.G. Wise, A.S. Weiss. Elastin signaling in wound repair. Birth Defects Res. C. Embryo Today 2012; 96(3):248-257.

4. P. Ashjian, et al. Noninvasive in situ evaluation of osteogenic differentiation by time-resolved laser-induced fluorescence spectroscopy. Tissue Engineering 2004;10(3-4):411-420.

5. L. Marcu, et al. Characterization of type I, I, I, IV, and V collagens by time-resolved laser-induced fluorescence spectroscopy. Proc. SPIE 2000; 3917. doi:10.1117/12.382720.

6. Rui Liu, et al. Compact, Non-invasive Frequency Domain Lifetime Differentiation of Collagens and Elastin. Sensors and Actuators B 2015; 219: 283-293.

7. Z. Deyl, et al. Studies on the chemical nature of elastin fluorescence. Biochim. Biophys. Acta. 1980;625(2):248-254.

8. D.R. Eyre, M.A. Paz, P.M. Gallop. Cross-linking in collagen and elastin. Annual Review of Biochemistry 1984; 53:717-748.

9. E. Fujimori. Changes induced by ozone and ultraviolet light in type I collagen: Bovine Achilles tendon collagen versus rat tail tendon collagen. Eur. J. Biochem. 1985; 152:299-306.

10. O. Vančíková, Z. Deyl. Disappearance of tyrosine residues in collagen with age. Suggestion of a possible reaction mechanism. Experimental Gerontology 1974; 9(3):123–130.

11. I. Miksík, Z. Deyl. Change in the amount of epsilon-hexosyllysine, UV absorbance, and fluorescence of collagen with age in different animal species. J. Gerontol. 1991; 46(3):B111-1116.

12. V.M. Monnier, R.R. Kohn, A. Cerami. Accelerated age-related browning of human collagen in diabetes mellitus. PNAS 1984; 81(2):583-587.

13. R. Meerwaldt, et al. Simple noninvasive measurement of skin autofluorescence. Ann. N. Y. Acad. Sci. 2005; 1043:290–298.

14. N. Krstajić, et al. 256 × 2 SPAD line sensor for time resolved fluorescence spectroscopy. Optics Express 2015, 23(5): 5653-5669.

15. D.K. Bird, et al. Simultaneous two-photon spectral and lifetime fluorescence microscopy.

Applied Optics 2004, 43(27): 5173-5182.

16. PP Provenzano, CT Rueden, SM Trier, L Yang, SM Ponik, DR Inman, PK Keely, KW Eliceriri. Nonlinear optical imaging and spectral-lifetime computational analysis of endogenous and exogenous fluorophores in breast cancer, Journal of Biomedical Optics 2008, 13(3), 031220-1.

17. J.R. Lakowicz. Principles of Spectroscopy. Third Edition. 2007; Springer, New York.

18. C. Zhang, et al. Open-Source 3D-Printable Optics Equipment. PLoS One 2013; DOI: 10.1371/journal.pone.0059840.

19. J. Wang, et al. Three-dimensional printing of tissue phantoms for biophotonic imaging. Optics Letters 2014; 39(10), p3010.

20. B. Berg, et al. Cellphone-Based Hand-Held Microplate Reader for Point-of-Care Testing of Enzyme-Linked Immunosorbent Assays. ACS Nano 2015; 9(8):7857–7866.

21. A. Forcucci, et al. All-plastic, miniature, digital fluorescence microscope for three part white blood cell differential measurements at the point of care. Biomedical Optics Express 2015; 6(11):4433-4446.

22. B.C. Gross, et al. Evaluation of 3D printing and its potential impact on biotechnology and the chemical sciences. Analytical Chemistry 2014; 86(7):3240-3253.

23. Y. Narukawa, et al. Ultra-high efficiency white light emitting diodes. Japanese Journal of Applied Physics 2006; 45(2):37–41.

24. M.R. Krames, et al. Status and future of high-power light-emitting diodes for solid-state lighting. Journal of Display Technology 2007; 3(2):160-175.

25. V. Mathiowetz, et al. Grip and pinch strength: normative data for adults. Arch. Phys. Med. Rehabil. 1985; 66(2):69-74.

26. J.R. Lakowizc, et al. Analysis of fluorescence decay kinetics from variable-frequency phase shift and modulation data. Biophys. J. 1984; 46:463-477.

27. M.Y. Berezin, S. Achilefu. Fluorescence lifetime measurements and biological imaging. Chem. Rev. 2010;110(5):2641–2684.

28. J.E. Phipps, et al. A fluorescence lifetime imaging classification method to investigate the collagen to lipid ratio in fibrous caps of atherosclerotic plaque. Lasers Surg. Med. 2012;44(7):564-571. doi: 10.1002/lsm.22059.

29. S. Ranjit, et al. Imaging Fibrosis and Separating Collagens using Second Harmonic Generation and Phasor Approach to Fluorescence Lifetime Imaging. Scientific Reports 2015; 5:13378.

# Chapter 4 Enabling FLIM for Histology: Facile and Stain-free Tissue Lifetime Imaging

## Introduction

### Monitoring protein glycation in diabetes

The wound healing process aims to repair damaged and open skin structures by depositing ECM proteins and changing their composition and crosslinking over time, a remodeling process that strengthens the tissue back to its normal biomechanical state [13-17]. Type I and III collagen, two key collagen forms in wound healing, have similar molecular structures, albeit thicker fiber bundles for type I collagen than type III. Type III collagen is deposited early in wound healing by fibroblast, and later remodeled and replaced by type I collagen, due to the stronger mechanical properties of its fibers [16, 17]. Based on our previous result, pure collagen III fibers exhibit longer lifetime than type I fibers (4 vs. 5 ns) [5, 6], which suggest that tissue lifetimes can be used to differentiate and monitor the process of wound healing.

Moreover, wound collagens can be modified by diabetes through protein glycation [18-24]. Diabetes, characterized by hyperglycemia, results in chronic complications of the eye [25, 26], nervous tissue [27-29], kidney [30-32], wound ulcers [33-35], and pervasive damage to the body's cardiovascular and peripheral vascular systems [36-39]. Specifically, elevated blood glucose increases protein glycation and leads to a gradual build-up of advanced glycation end-products (AGEs) in tissue [39-42]. AGEs further induce ROS formation [38, 40, 41], resulting in oxidative damage, protein crosslinking, inflammation, and decreased cell proliferation [43-47]. AGE related damage, in addition to an already poor microvasculature and impaired cell

recruitment [34, 35, 46, 48, 49], contributes to improper wound healing in diabetes. This is especially acute in body extremities like the foot, where the aforementioned problems are exacerbated by the lack of circulation, leading to non-healing wounds—e.g. diabetic foot ulcers.

Incidentally, pentosidine—a major AGE species derived from collagen crosslinking [50-53]—is also a prominent fluorophore with modified lifetime signature compared to collagen [52-53]. Therefore, lifetime measurements of ECM components of collagen I, III, elastin, and their modification by the addition of pentosidine can provide a set of standards for lifetime-based tissue histology. Furthermore, these measurements were extended to the imaging of a full-thickness diabetic foot ulcer, demonstrating a label-free and disease-specific imaging modality that can complement standard collagen histology and immunohistochemistry.

## Method

### LED tissue lifetime imaging system

We have previously demonstrated frequency domain based collagen detections [5], including a 3D printed microoptics system [6]. Here we extended the technique to an imaging modality for lifetime-based tissue histology. Moreover, we elected to use scanning imaging in lieu of wide-field imaging to avoid complicated gated imager. This enabled the realization of a compact, upright LED modulated scanning microscope, Fig. 1, with components costing less than $17k USD (Supplmentary Table 1). In this system, light from a 1 mm2 emitter (Thorlabs DC3100-365) is continuously modulated at 20 MHz and coupled into the microscope optical train via a 275-375 nm band pass filter and a 4X, 0.15 NA objective (Amscope). This light is redirected via a 400 nm dichroic to a 60X imaging objective and projected at the sample plane with a spot size of around 78 microns FWHM (full width at half max). The objective allows over 3 mm of working space for the sample to be scanned on a stage driven by x-y

linear stepper motors (Thorlabs KST101). The scanning is set at a constant speed (2.5 mm/s) and scans continuously in an S-shaped raster scan path, Fig. 1. The emission is imaged by the same 60X objective through the dichroic and filtered by a 400 nm emission filter before being focused onto an avalanche photodiode (Thorlabs APD120A2). Alternatively, a CCD camera can be placed between the filters and photodiode via a 45° mirror to allow visual focusing and spot size measurements. A digitizer (Picoscope 6404C) acquires data points from the photodiode with refresh rate of 28.9 Hz. Each acquisition point represents the emission lifetime of a 78 micron diameter spot on the sample.

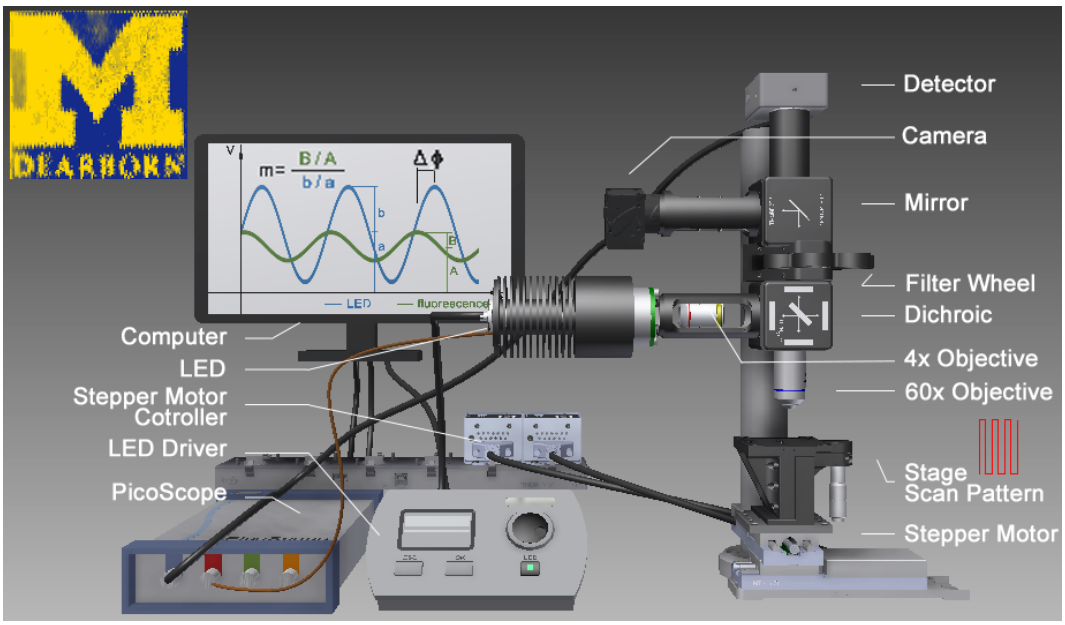


**Figure 15. System schematic.** The system including LED, objectives, filters and dichroic, digital camera, stepper motor and controller, digitizer, and computer in an up right designed for histological measurement of tissue. Using a raster scanning pattern, a 6 by 6 mm M logo (top left corner) printed on paper was imaged using the $17k USD system.

### System Characterization

The final design of the microscope optics shown in Fig. 1 was realized via three system characterizations. First, the system was modeled by ray tracing (Trace Pro, Lambda Research) to understand the theoretical spot sizes of the excitation and emission intensities. Next, the

actual spot sizes were measured with various combinations of collection and imaging objectives. The results were plotted as a function of the etendues, or geometric extends, of the collection and imaging objectives. Objective combination yielding excitation spot with the appropriate intensity and FWHM size was selected. Finally, the data acquisition protocol was optimized for the best scanning speed at the selected spot size.

**Biophotonics Measurements**

Measurements using the LED tissue lifetime imaging system was demonstrated first by establishing a biophotonic model of diabetic skin wound, then by imaging a diabetic foot ulcer. For the diabetic wound model, fluorescence lifetimes of extra cellular matrix (ECM) proteins and their combination with AGE's were measured. Purified fibrous Collagen I and III, and solid elastin powder were included as major ECM proteins (Sigma Aldrich). Pentosidine in PBS (Fisher BioReagents) was selected as the prominent autofluorescent AGE component in skin [52, 53]. Pentosidine was added to the ECM proteins at 7 μg/mg protein ratio according to reported in vivo skin compositions [52], and dried overnight for combined measurements. Next, a diabetic foot ulcer was imaged. This 3 cm by 3cm full thickness donor tissue (71 years old male, type I diabetes) was obtained from Tissue for Research Ltd, frozen in -80°C. The approximately 3 by 3 cm ulcer area was cut into 9 squares for imaging individually, and the combined frames were combined into a collage for display.

**Data acquisition and analysis**

All frequency domain modulation was applied at 20 MHz via the 365 nm LED (Thorlabs DC3100-365). Data acquisition was triggered via the LED output and recorded on an USB digitizer (Picoscope 6404C) at 1.25 GSps. Recorded data was averaged prior to the Fourier transform frequency analysis. To average the data, the data set was truncated into lengths of

1250 data points (which allows fundamental frequency to hit 20 MHz), each offset by 2π phase or one period apart. For example, a 10k data set will provide 140X averages of the 1250 point long data length. The averaged data was then Fourier transformed to analyze the magnitude and phase of the signal at 20 MHz compared. The demodulation and phase lifetimes are calculated using these FFT components and fitted to a multi-exponential model as described in our previous publications [5, 6]. Three lifetime measurements were recorded per image pixel per acquisition.

## Result and discussion

### Optical ray tracing

Ray tracing was employed to model the theoretical excitation and emission spot sizes, Figure 16. The system was separated into the excitation and emission paths. The image of the excitation spot at the sample plane, Figure 16A, was carried forward to the emission path to produce the spot at the detector plane, Figure 16B. The 4X-60X objective pair resulted in an excitation spot smaller than 100 μm and an emission spot that matches the 1 mm diameter of the avalanche photodiode's active area.

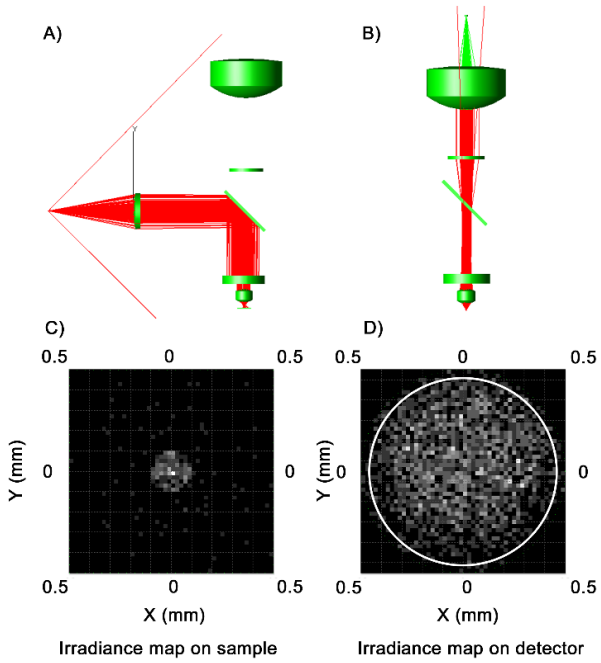


**Figure 16. Ray tracing modeling.** A) ray tracing of emission arm. 365 nm light from LED is collimated by 4x objective and reflected by 400 nm dichroic. Then the reflected collimated light goes through 60x objective (including aperture), and focuses on sample. B) ray tracing of excitation arm. Fluorescence collimated by 60x objective with wavelength over 400 nm pass through dichroic and 400 nm long pass filter to filter out reflection, focus on detector though lens.

**Etendue and spot size characterization**

The image of the excitation spot at the sample plane is a result of the reduction ratio between the collection and imaging objectives. Moreover, the amount of light coupled through these objectives ultimately affects the intensity of the resultant spot. this light coupling can be expressed in terms of the geometry extend, or etendue G:

$$G = \pi S NA^2$$

Where S is the cross sectional area in mm2 and NA is the numerical aperture. To characterize the system, the optical power was plotted as a function of the etendue of each objective. For a fixed imaging objective, the optical power increases exponentially versus the collection objective's etendue, Figure 17A. However, the etendue coefficient (ratio of imaging to collection etendue) shows a maximum versus the collection etendue, beyond which the throughput is limited by the imaging objective. For a fixed collection objective, the optical

power also increases exponentially with the imaging objective's etendue, Figure 17B. Here, the rise of optical power is more sensitive to the imaging etendue than the collection etendue, consistent with the observation that throughput is limited by the imaging objective.

To select the combination of objectives that produces a small and bright excitation spot, the maximum CCD count per integration time was plotted against the measured FWHM diameter, Figure 17C. Both intensity and etendue coefficient were optimized for spot sizes between 60-80 µm. Finally, the objective combination of 4X and 60X was selected for maximum intensity with a spot size of 78 µm, Figure 17D. This spot size allowed us to scan at a conservative pixel resolution of 100 by 100 µm, used in all of the scanning results shown in subsequent data.

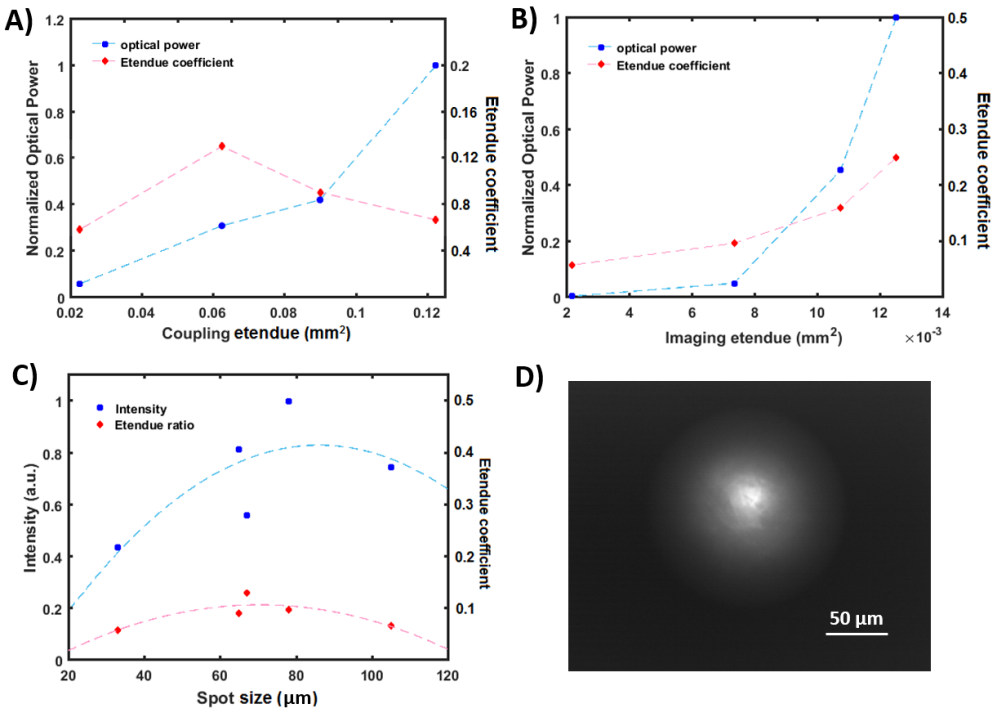


**Figure 17. Etendue and spot size characterization.** A) Using the same imaging objective, normalized optical power increases exponentially while the etendue coefficient shows a maximum beyond which throughput is limited by the imaging objective. B) Using the same collection objective, both power and etendue coefficient increases exponentially as a function of the imaging objective's etendue. C) The intensity and etendue coefficient were both optimized for a spot size between 60-80 µm. D) We selected a spot size of 78 µm produced by a combination of 4X and 60X collection and imaging objectives, respectively.

**Stage calibration**

The imaging speed is limited by the scanning speed of the stage, which is dependent on the acquisition speed of the digitizer (Picoscope 6404C). Moreover, the digitizer's speed of acquisition is inversely proportional to the chosen buffer size. Therefore, the buffer size was varied to examine its effect on the data acquisition rate and the resultant data quality (i.e. standard deviation) as shown in Figure 18. As expected, the larger the selected buffer size, the slower the acquisition rate (pixel per second). However, larger buffer size allows for more data averaging, which reduces the data noise in terms of standard deviation. As shown in Figure 18, standard deviation of the data increases sharply when buffer size is less than 10k, while the acquisition rate flattens out below the same 10k buffer size. Below 10k buffer size, data acquisition is limited by the time it takes the digitizer to turn on and off. To balance the scanning speed versus data quality, we choose 10k as our minimum buffer size for data acquisition. For a sample area of 5 mm by 5 mm at 100 µm resolution, the scanning would take approximately 15 minutes. Up to 1.4 cm by 1.4 cm area has been achieved here, for the diabetic ulcer imaging presented in subsequent results.

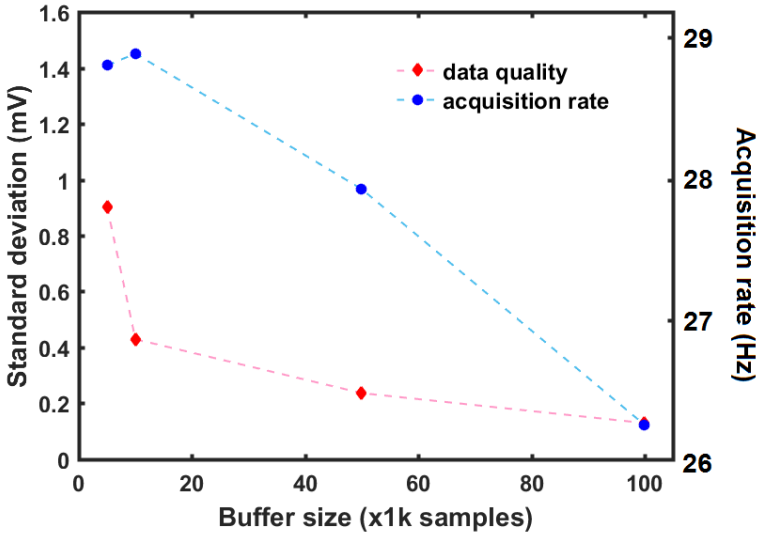


**Figure 18. Data acquisition rate and standard deviation versus buffer size.** Buffer size is inversely related to data acquisition rate and standard deviation (a measure of data noise).

However, above 10k buffer the standard deviation does not appreciatively decrease while below 10k the scanning speed is limited by the digitizer's on/off rate. Thus, 10k was selected to be the optimal buffer size used in all subsequent scanning.

**Biophotonic model of diabetic wound**

To understand the components of the diabetic wound, we applied the LED tissue lifetime imaging system to scan purified ECM and AGE (pentosidine) samples to characterize their individual and combined lifetimes, Figure 19. The lifetimes of pure ECM proteins were 3.9±0.012, 4.2±0.049, and 6.3±0.081 ns for collagen I, III, and elastin, respectively, and agreed with our previous reported values [5, 6]. The pentosidine AGE by itself presented a lifetime of 3.2±0.61 ns. With AGE incubation, the ECM lifetimes were lowered to 3.7±0.21, 4.0±0.25, and 5.6±0.17 ns, respectively. This measurement suggests that AGE in diabetic skin would lower the apparent lifetime values of both normal (predominant type I collagen) and wound (predominantly type III collagen) tissues.

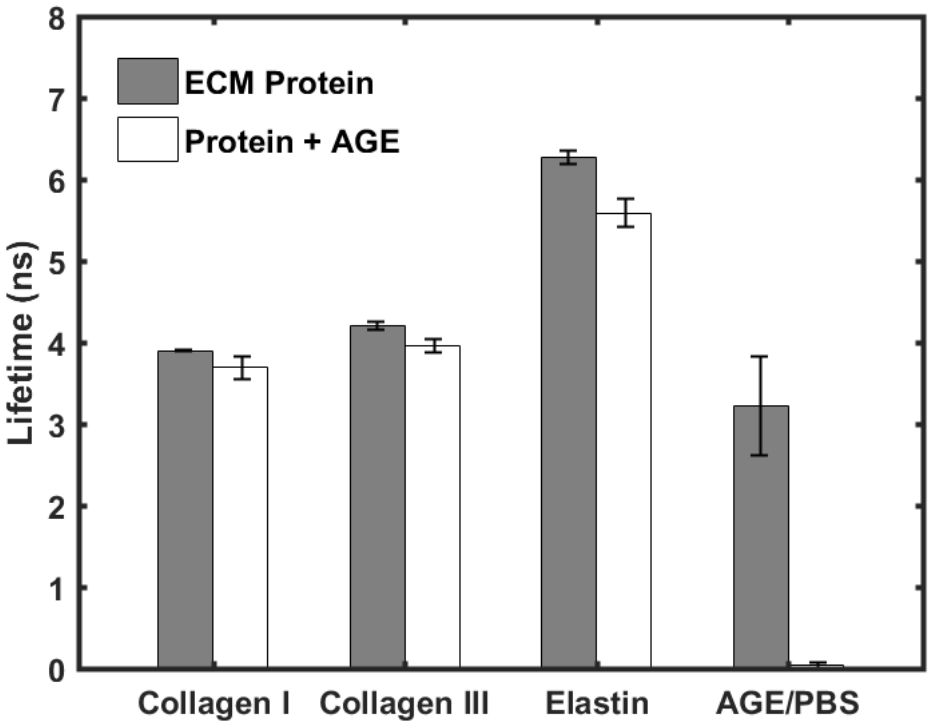


**Figure 19. Intrinsic lifetimes of ECM proteins and their modification by pentosidine**

**(AGE).** Collagen I, III, and elastin lifetimes were measured with and without the incubation of pentosidine as the major fluorescent advanced glycation end-product in the skin. Type III collagen lifetime was higher than type I both before and after the incubation. And the all ECM proteins + AGE combinations exhibited lowered lifetimes after incubation with AGE. Pentosidine in solution yielded the lowest measurable lifetimes while PBS has negligible fluorescence intensity.

**Imaging diabetic foot ulcer**

To enable stain-free imaging of the diabetic foot ulcer, 9 square areas were imaged individually and the resultant frames were combined to form a collage for presentation, Figure 20. The ring around the ulcer has low intensity, leading to noisy lifetime values. A threshold was applied to remove these values from display. Within this ring, the ulcer tissue displayed a higher lifetime of $4.4 \pm 0.36$ ns compared to a $3.72 \pm 0.45$ ns lifetime of the unwounded tissue outside, $p<0.02$. The longer lifetime is consistent with our previously reported trend between type III and type I collagens [5,6], indicating a non-healing wound, i.e. an ulcer. Moreover, it can be seen that the unwounded tissue has shorter lifetime than pure collagen I protein from Figure 19, with values closer to that of collagen I + AGE (3.6 vs. 3.7 ns). For reference, normal skin tissue has a measured lifetime of $3.9 \pm 0.07$ ns. This fits our model of AGE modified diabetic skin. However, the lifetime of the wound area is closer to that of unmodified collagen III protein (4.4 vs. 4.2 ns), suggesting that the ulcer in our sample may not be affected by AGE to the same degree as unwounded tissue. This result demonstrates the potential of the LED tissue lifetime imaging in discriminating diabetic wounds and ulcers using a biophotonic model composed of ECM and AGE proteins.

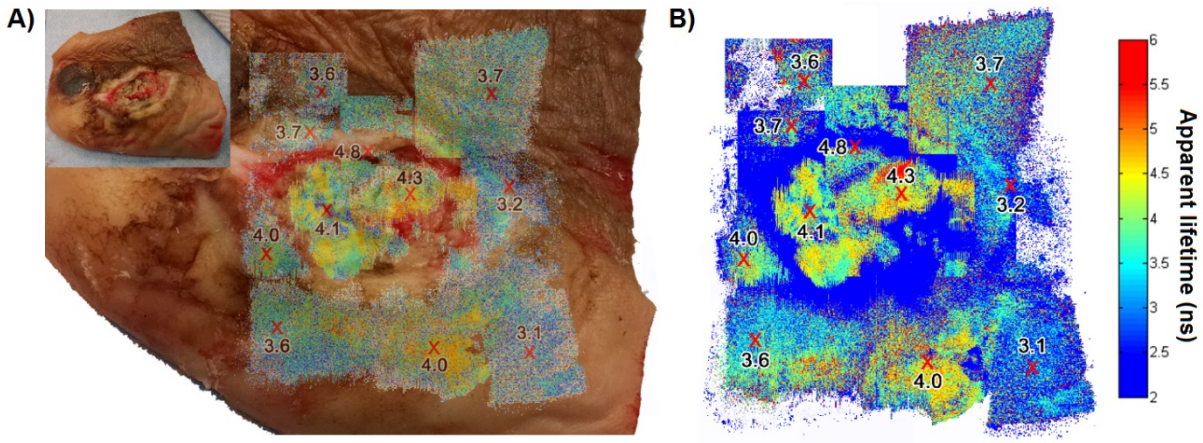


**Figure 20. LED tissue lifetime imaging of diabetic foot ulcer.** A) A full thickness diabetic foot ulcer (3 by 3 cm) was obtained and cut into 9 squares (overlay) for label-free collagen imaging. B) The pseudo colored lifetime map shows that ulcer tissue has higher lifetime than surrounding unwounded tissue. Moreover, the unwounded tissue has lower lifetime than normal skin with predominantly type I collagen, suggesting that unwounded diabetic skin is more affected by pentosidine as an AGE than the ulcer tissue.

## Future Works

In this work the scanning of a 1 cm by 1 cm sample area, similar size to a single histological section, takes roughly 40 minutes to complete. This should be taken into context of the staining and labeling protocols, e.g. picro Sirius stain and immunochemistry prep, which takes up to half a day to complete. However, to enable faster scanning, wide-field imaging has to be considered. Due to the lowered frequency and simple sinusoidal modulation, we plan to build simplified gating circuits with off-the-shelf ocular image intensifiers in front of CMOS sensors, rather than using the more complicated ICCD (intensified charged-coupled device) imagers for wide-field applications. Additionally, collagen imaging can be enhanced with the spectral-lifetime techniques we previously developed for point detections [6]. Lastly, the electronic components can be consolidated into a single enclosure, with a GUI (graphical user interface) wrapped script to automate the microscopy and further simplify user operations.

## Summary

A LED based tissue lifetime imaging system was constructed and automated for the detection

of ECM proteins and their modification by pentosidine in diabetic wounds. The system was capable of scanning large centimeter squared areas with 100 μm pixel resolution (78 μm FWHM spot size). Using this system, collagen I, III, and elastin proteins with and without pentosidine were measured, showing that their lifetimes were lowered by the AGE incubations. This is also observed in our diabetic foot ulcer imaging, where the normal skin shows greater lifetime suppression by AGE than the ulcer itself. Beyond wound healing and diabetes, a number of collagen and ECM related diseases can be imaged by our label-free microscopy—scarring, tissue fibrosis, tumor demarcation, and tissue inflammation diseases. By providing a quantifiable, more nuance model of tissue biophotonics while dramatically lower the cost of instrumentation, the LED tissue lifetime system hopes to increase accessibility and popularity of label free collagen imaging for clinical histology applications.

**References**


1. Z. Deyl, et al. Studies on the chemical nature of elastin fluorescence. Biochim. Biophys. Acta. 1980;625(2):248-254.

2. D.R. Eyre, M.A. Paz, P.M. Gallop. Cross-linking in collagen and elastin. Annual Review of Biochemistry 1984; 53:717-748.

3. E. Fujimori. Changes induced by ozone and ultraviolet light in type I collagen: Bovine Achilles tendon collagen versus rat tail tendon collagen. Eur. J. Biochem. 1985; 152:299-306

4. O. Vančíková, Z. Deyl. Disappearance of tyrosine residues in collagen with age. Suggestion of a possible reaction mechanism. Experimental Gerontology 1974; 9(3):123–130.

5. R. Liu, et al. Compact, Non-invasive Frequency Domain Lifetime Differentiation of Collagens and Elastin. Sensors and Actuators B 2015; 219: 283-293.

6. Zou L, Koslakiewicz R, Mahmoud M, Fahs M, Liu R, Lo JF. Three-dimensional printed miniaturized spectral system for collagen fluorescence lifetime measurements. Journal of biomedical optics. 2016 Jul 1;21(7):075001-.

7. Marcu L, Cohen D, Maarek JM, Grundfest WS. Characterization of type I, II, III, IV, and V collagens by time-resolved laser-induced fluorescence spectroscopy. Optical Biopsy III. 2000 Jan 23;3917:93-101.

8. Berezin MY, Achilefu S. Fluorescence lifetime measurements and biological imaging. Chemical reviews. 2010 Mar 31;110(5):2641-84.

9. Phipps JE, Sun Y, Fishbein MC, Marcu L. A fluorescence lifetime imaging classification method to investigate the collagen to lipid ratio in fibrous caps of atherosclerotic plaque. Lasers in surgery and medicine. 2012 Sep 1;44(7):564-71.

10. Ranjit S, Dvornikov A, Stakic M, Hong SH, Levi M, Evans RM, Gratton E. Imaging fibrosis and separating collagens using second harmonic generation and phasor approach to fluorescence lifetime imaging. Scientific reports. 2015 Aug 21;5:13378.

11. J.R. Lakowicz. Principles of Spectroscopy. Third Edition. 2007; Springer, New York.

12. Lakowicz JR, Laczko G, Cherek H, Gratton E, Limkeman M. Analysis of fluorescence decay kinetics from variable-frequency phase shift and modulation data. Biophysical journal. 1984 Oct 1;46(4):463-77.

13. I.A. Darby, T.D. Hewitson. Fibroblast differentiation in wound healing and fibrosis. International Review of Cytology 2007;257:143-179.

14. H.P. Ehrlich. The role of connective tissue matrix in wound healing. Prog. Clin. Biol. Res. 1988;266:243–258.

15. M.J. Ranzer, L. Chen, L.A. DiPietro. Fibroblast function and wound breaking strength are impaired by acute ethanol intoxication. Alcohol Clin. Exp. Res. 2011;35:83-90.

16. J.R. Merkel, B.R. DiPaolo, G.G. Hallock, D.C. Rice. Type I and type III collagen content of healing wounds in fetal and adult rats. Proceedings of the Society of Experimental Biology and Medicine 1988;187:493-497.

17. J.F. Almine, S.G. Wise, A.S. Weiss. Elastin signaling in wound repair. Birth Defects Res. C. Embryo Today 2012;96(3):248-257.

18. Gkogkolou P, Böhm M. Advanced glycation end products: Key players in skin aging?. Dermato-endocrinology. 2012 Jul 1;4(3):259-70.

19. Van Putte L, De Schrijver S, Moortgat P. The effects of advanced glycation end products (AGEs) on dermal wound healing and scar formation: a systematic review. Scars, Burns & Healing. 2016 Nov 30;2:2059513116676828.

20. Singh R, Barden A, Mori T, Beilin L. Advanced glycation end-products: a review. Diabetologia. 2001 Feb 1;44(2):129-46.

21. Ahmed N. Advanced glycation endproducts—role in pathology of diabetic complications. Diabetes research and clinical practice. 2005 Jan 31;67(1):3-21.

22. Huijberts MS, Schaper NC, Schalkwijk CG. Advanced glycation end products and diabetic foot disease. Diabetes/metabolism research and reviews. 2008 May 1;24(S1).

23. Goova MT, Li J, Kislinger T, Qu W, Lu Y, Bucciarelli LG, Nowygrod S, Wolf BM, Caliste X, Yan SF, Stern DM. Blockade of receptor for advanced glycation end-products restores effective wound healing in diabetic mice. The American journal of pathology. 2001 Aug 31;159(2):513-25.

24. Goova MT, Li J, Kislinger T, Qu W, Lu Y, Bucciarelli LG, Nowygrod S, Wolf BM, Caliste X, Yan SF, Stern DM. Blockade of receptor for advanced glycation end-products restores effective wound healing in diabetic mice. The American journal of pathology. 2001 Aug 31;159(2):513-25.

25. Wilkinson CP, Ferris FL, Klein RE, Lee PP, Agardh CD, Davis M, Dills D, Kampik A, Pararajasegaram R, Verdaguer JT, Group GD. Proposed international clinical diabetic retinopathy and diabetic macular edema disease severity scales. Ophthalmology. 2003 Sep 30;110(9):1677-82.

26. Aiello LP, Avery RL, Arrigg PG, Keyt BA, Jampel HD, Shah ST, Pasquale LR, Thieme H, Iwamoto MA, Park JE, Nguyen HV. Vascular endothelial growth factor in ocular fluid of patients with diabetic retinopathy and other retinal disorders. New England Journal of Medicine. 1994 Dec 1;331(22):1480-7.

27. Malik RA, Tesfaye S, Thompson SD, Veves A, Sharma AK, Boulton AJ, Ward JD. Endoneurial localisation of microvascular damage in human diabetic neuropathy. Diabetologia. 1993 May 1;36(5):454-9.

28. Vincent AM, Callaghan BC, Smith AL, Feldman EL. Diabetic neuropathy: cellular mechanisms as therapeutic targets. Nature Reviews Neurology. 2011 Oct 1;7(10):573-83.

29. Edwards JL, Vincent AM, Cheng HT, Feldman EL. Diabetic neuropathy: mechanisms to management. Pharmacology & therapeutics. 2008 Oct 31;120(1):1-34.

30. Johnson RJ, Segal MS, Sautin Y, Nakagawa T, Feig DI, Kang DH, Gersch MS, Benner S, Sánchez-Lozada LG. Potential role of sugar (fructose) in the epidemic of hypertension, obesity and the metabolic syndrome, diabetes, kidney disease, and cardiovascular disease. The American journal of clinical nutrition. 2007 Oct 1;86(4):899-906.

31. Brenner BM, Cooper ME, de Zeeuw D, Keane WF, Mitch WE, Parving HH, Remuzzi G, Snapinn SM, Zhang Z, Shahinfar S. Effects of losartan on renal and cardiovascular outcomes in patients with type 2 diabetes and nephropathy. New England Journal of Medicine. 2001 Sep 20;345(12):861-9.

32. Parving HH, Smidt U, Andersen A, Svendsen P. Early aggressive antihypertensive treatment reduces rate of decline in kidney function in diabetic nephropathy. The Lancet. 1983 May 28;321(8335):1175-9.

33. Falanga V. Wound healing and its impairment in the diabetic foot. The Lancet. 2005 Nov 18;366(9498):1736-43.

34. Lu D, Chen B, Liang Z, Deng W, Jiang Y, Li S, Xu J, Wu Q, Zhang Z, Xie B, Chen S. Comparison of bone marrow mesenchymal stem cells with bone marrow-derived mononuclear cells for treatment of diabetic critical limb ischemia and foot ulcer: a double-blind, randomized, controlled trial. Diabetes research and clinical practice. 2011 Apr 30;92(1):26-36.

35. Barcelos LS, Duplaa C, Kränkel N, Graiani G, Invernici G, Katare R, Siragusa M, Meloni M, Campesi I, Monica M, Simm A. Human CD133+ progenitor cells promote the healing of diabetic ischemic ulcers by paracrine stimulation of angiogenesis and activation of Wnt signaling. Circulation research. 2009 May 8;104(9):1095-102.

36. Stratton IM, Adler AI, Neil HA, Matthews DR, Manley SE, Cull CA, Hadden D, Turner RC, Holman RR. Association of glycaemia with macrovascular and microvascular complications of type 2 diabetes (UKPDS 35): prospective observational study. Bmj. 2000 Aug 12;321(7258):405-12.

37. Adler AI, Boyko EJ, Ahroni JH, Smith DG. Lower-extremity amputation in diabetes. The independent effects of peripheral vascular disease, sensory neuropathy, and foot ulcers. Diabetes care. 1999 Jul 1;22(7):1029-35.

38. Jay D, Hitomi H, Griendling KK. Oxidative stress and diabetic cardiovascular complications. Free Radical Biology and Medicine. 2006 Jan 15;40(2):183-92.

39. Park L, Raman KG, Lee KJ, Lu Y, Ferran LJ, Chow WS, Stern D, Schmidt AM. Suppression of accelerated diabetic atherosclerosis by the soluble receptor for advanced glycation endproducts. Nature medicine. 1998 Sep 1;4(9).

40. Goh SY, Cooper ME. The role of advanced glycation end products in progression and complications of diabetes. The Journal of Clinical Endocrinology & Metabolism. 2008 Apr 1;93(4):1143-52.

41. Yao D, Brownlee M. Hyperglycemia-induced reactive oxygen species increase expression of the receptor for advanced glycation end products (RAGE) and RAGE ligands. Diabetes. 2010 Jan 1;59(1):249-55.

42. Giardino I, Edelstein D, Brownlee M. BCL-2 expression or antioxidants prevent hyperglycemia-induced formation of intracellular advanced glycation endproducts in bovine endothelial cells. Journal of Clinical Investigation. 1996 Mar 15;97(6):1422.

43. Basta G, Schmidt AM, De Caterina R. Advanced glycation end products and vascular inflammation: implications for accelerated atherosclerosis in diabetes. Cardiovascular research. 2004 Sep 1;63(4):582-92.

44. Brownlee M, Vlassara H, Kooney A, Ulrich P, Cerami A. Aminoguanidine prevents diabetes-induced arterial wall protein cross-linking. Science. 1986 Jun 27;232:1629-33.

45. Candido R, Forbes JM, Thomas MC, Thallas V, Dean RG, Burns WC, Tikellis C, Ritchie RH, Twigg SM, Cooper ME, Burrell LM. A breaker of advanced glycation end products attenuates diabetes-induced myocardial structural changes. Circulation research. 2003 Apr 18;92(7):785-92.

46. Wang K, Zhou Z, Zhang M, Fan L, Forudi F, Zhou X, Qu W, Lincoff AM, Schmidt AM, Topol EJ, Penn MS. Peroxisome proliferator-activated receptor γ down-regulates receptor for advanced glycation end products and inhibits smooth muscle cell proliferation in a diabetic and nondiabetic rat carotid artery injury model. Journal of Pharmacology and Experimental Therapeutics. 2006 Apr 1;317(1):37-43.

47. Alikhani M, Alikhani Z, Boyd C, MacLellan CM, Raptis M, Liu R, Pischon N, Trackman PC, Gerstenfeld L, Graves DT. Advanced glycation end products stimulate osteoblast apoptosis via the MAP kinase and cytosolic apoptotic pathways. Bone. 2007 Feb 28;40(2):345-53.

48. Loots MA, Lamme EN, Zeegelaar J, Mekkes JR, Bos JD, Middelkoop E. Differences in cellular infiltrate and extracellular matrix of chronic diabetic and venous ulcers versus acute wounds. Journal of Investigative Dermatology. 1998 Nov 30;111(5):850-7.

49. Gallagher KA, Liu ZJ, Xiao M, Chen H, Goldstein LJ, Buerk DG, Nedeau A, Thom SR, Velazquez OC. Diabetic impairments in NO-mediated endothelial progenitor cell mobilization and homing are reversed by hyperoxia and SDF-1α. Journal of Clinical Investigation. 2007 May 1;117(5):1249.

50. Sajithlal GB, Chithra P, Chandrakasan G. Effect of curcumin on the advanced glycation and cross-linking of collagen in diabetic rats. Biochemical pharmacology. 1998 Dec 15;56(12):1607-14.

51. Verzijl N, DeGroot J, Zaken CB, Braun- Benjamin O, Maroudas A, Bank RA, Mizrahi J, Schalkwijk CG, Thorpe SR, Baynes JW, Bijlsma JW. Crosslinking by advanced

glycation end products increases the stiffness of the collagen network in human articular cartilage: a possible mechanism through which age is a risk factor for osteoarthritis. Arthritis & Rheumatology. 2002 Jan 1;46(1):114-23.

52. Dyer DG, Blackledge JA, Thorpe SR, Baynes JW. Formation of pentosidine during nonenzymatic browning of proteins by glucose. Identification of glucose and other carbohydrates as possible precursors of pentosidine in vivo. Journal of Biological Chemistry. 1991 Jun 25;266(18):11654-60.

53. Meerwaldt R, Hartog JW, Graaff R, Huisman RJ, Links TP, den Hollander NC, Thorpe SR, Baynes JW, Navis G, Gans RO, Smit AJ. Skin autofluorescence, a measure of cumulative metabolic stress and advanced glycation end products, predicts mortality in hemodialysis patients. Journal of the American Society of Nephrology. 2005 Dec 1;16(12):3687-93.

54. Fantini S, FRANCESCHINIFANTINI M, Maier J, Walker S, Barbieri B, Gratton E. Frequency-domain multichannel optical-detector for noninvasive tissue spectroscopy and oximetry. Optical Engineering. 1995 Jan 1;34(1).

55. Elder AD, Frank JH, Swartling J, Dai X, Kaminski CF. Calibration of a wide- field frequency- domain fluorescence lifetime microscopy system using light emitting diodes as light sources. Journal of microscopy. 2006 Nov 1;224(2):166-80.

56. Yuan B, McClellan SR, Al-Mifgai BF, Growney EA, Komolafe OA. A cost-efficient frequency domain fluorescence lifetime measurement system. American Journal of Physics. 2010 Jan;78(1):28-34.

57. O'Hagan WJ, McKenna M, Sherrington DC, Rolinski OJ, Birch DJ. MHz LED source for nanosecond fluorescence sensing. Measurement Science and Technology. 2001 Dec 4;13(1):84.

# Chapter 5 Conclusion

There have been technical breakthroughs in tissue histology and collagen detection in the forms of FLIM, SHG (second harmonic generation), and collagen autofluorescence detection. However, these advancements did not break through the standard mold of tissue histology, and often times require the same, if not more, sample preparation through tissue labeling and immunohistochemistry. What this thesis has achieved is the development of a new frequency domain technique for tissue ECM discrimination, and the realization of a number of instrumentation that facility its applications as a point-of-care, benchtop, or imaging microcopy modality. Furthermore, the work has generated a body of published data on the intrinsic lifetimes of collagen I, III, elastin, and their pentosidine modified counterparts. This forms a necessary biophotonic model for the interpretation of raw, composite lifetimes measured from tissues. Furthermore, by creating the suite of easily accessible devices, these works broaden the appeal of the technique for numerous clinical and biomedical research laboratories that may have great interest, but do not desire the complicacies associated with traditional instrumentations. From these works, several key areas are identified that require future work. The electronics integration is a key component in the miniaturization and simplification of the instrumentation, important from a usability perspective for clinical researchers. Next the spectral and lifetime optimization gained from our work needs to be implemented in a automatic manner, through additional software and embedded programming. Lastly, a new method of gating wide-field imaging should be considered, for example using gating

intensifiers from night-vision gaggles. In addition to these future works, the hope is to continue the motivation behind this thesis towards further implementation and clinical applications of the frequency domain tissue lifetime technique.